Trans-ruthenium(II) complexes for photoactivated cChemotherapy: from design to anticancer activity

Verbeet, W.

Chapter 4

Dual targeting of NAMPT and tubulin with *trans* ruthenium-based photoactivated chemotherapy complexes

Abstract: Here, a series of *trans*-tetrapyridyl ruthenium(II) complexes $[Ru(MeL)(L')(L'')]^{2+}$ is reported, where MeL = di([2,2'-bipyrid]-6-yl)-N-methylamine, from which the axial ligand L' and L" can be photosubstituted upon irradiation with visible light. Two identical or different axial ligands were considered, i.e. the nicotinamide phosphoribosyl transferase (NAMPT) inhibitor STF31 and/or microtubule polymerization inhibitor MTI were incorporated, resulting in three complexes: $[Ru(MeL)(STF31)_2]^{2+}$ ($[\mathbf{1}]^{2+}$), $[Ru(MeL)(MTI)_2]^{2+}$ ($[\mathbf{2}]^{2+}$), and $[Ru(MeL)(STF31)(MTI)]^{2+}$ ($[\mathbf{3}]^{2+}$). Distinct differences in photoreactivity were observed for $[\mathbf{1}]^{2+}$ – $[\mathbf{3}]^{2+}$ upon irradiation with blue, green or red light in aqueous solution. Strikingly, red light irradiation resulted in selective photosubstitution of STF31 from the dissymmetric complex $[\mathbf{3}]^{2+}$, which allowed for wavelength–dependent sequential release of both inhibitors: red light released STF31, followed by blue light released MTI. *In vitro* evaluation of a STF31:MTI co-treatment in a 1:1 molar ratio in skin melanoma (A375), lung adenocarcinoma (A549) and glioblastoma (U87MG and U251) cell lines in normoxia (21% O_2) and hypoxia (>1% O_2) revealed a synergistic effect and EC_{50} < 2.0 µM. The three complexes $[\mathbf{1}]^{2+}$ – $[\mathbf{3}]^{2+}$ were also evaluated in the same cell lines. While for $[\mathbf{2}]^{2+}$ minimal photocytotoxicity was found when activated with green or red light, photoactivation of $[\mathbf{1}]^{2+}$ and $[\mathbf{3}]^{2+}$ resulted in an increased toxicity up to 33–fold. Strikingly, synergistic cell killing of the 1:1 mixture of free drugs STF31:MTI was also observed when $[\mathbf{3}]^{2+}$ was activated with green light, while the photocytotoxicity of this complex was found to be O_2–independent. The exceptional photochemical and *in vitro* properties of $[\mathbf{3}]^{2+}$ underline the potential of such dual-targeting PACT compounds for the treatment of hypoxic tumors.

This work will be published as a full paper: W. Verbeet, S. K. Götzfried, A. Kornienko, S. Bonnet, *manuscript in preparation*

4.1 Introduction

The main challenges for chemotherapy treatment of human malignancies arises from systemic toxicity in patients due to off-targets, as well as from the development of drug resistance. To avoid these issues as much as possible, the simultaneous use of two or more chemotherapeutic agents, often referred to as "combination chemotherapy", has become the standard-of-care in clinical cancer treatment.[1] Since the first successful application of combination therapy in the mid-1960's against acute lymphoblastic leukemia, the concept has been applied in most clinical treatments.[2] Combination therapy generally leads to an enhanced therapeutic effect through synergy, reaching a higher antitumor activity while lowering the individual dose of each component of the combination, thereby reducing side-effects, compared to high-dose monotreatment. Though the experience of oncologists with combination therapy keeps progressing, the ability to rationally design a synergistic combination of drugs remains a challenge, due to the limited comprehension of fundamental cellular processes in cancer and of the mode-of-action of many anticancer drugs.[3] High-throughput or computational library screening are therefore often needed to elucidate potential combination candidates.[4] With the recent developments in artificial intelligence, machine learning methods are gaining popularity to predict potential drug synergies through computational modelling.[5] Nonetheless, combination therapies may still suffer from deleterious side-effects or efficacy issues resulting from one of the components not reaching the targeted location at the same time as the other one, thereby drastically limiting their synergy.[6] In some cases, liposomal or nanoparticle–based formulations can improve the bioavailability of the drug mixtures and ensure the simultaneous delivery of two or more drugs.[7] However, nano-formulations are not as chemically homogenous as molecular drugs, and do not penetrate cells via the same mechanisms as the drugs they contain. Binary molecular prodrugs have also been proposed, in which two biologically active moieties are connected molecularly by a labile linker that is sensitive to the cancer-associated microenvironment such as the lower pH, the presence of high oxidative stress, or the overexpression of specific enzymes.[8,9] However, side-effects might occur due to non-specific cleavage of the linker, which motivates the use of light for the controlled release of two active pharmaceutical components from a single prodrug.

For single-component therapies, light-activated prodrugs are frequently utilized to increase the tumor selectivity and minimize interaction with off-targets before the (pro)drug reaches its target An example of this strategy is found in ruthenium-based photoactivated chemotherapy (PACT), in which a ruthenium-based "caged" prodrug dissociates upon visible-light irradiation, thus releasing a biologically active species.[10] While the potential of PACT has been demonstrated *in vitro* by numerous groups,[11–13] and more recently *in vivo,*[14,15] this strategy is generally focuses on the light-induced release of a single chemotherapeutic agent. The integration of the PACT concept with the idea of combination

therapy could lead to a new jump in the antitumor efficacy of these molecules, for example to address the challenging targets of hypoxic tumors. In such an approach, enhanced potency can be achieved between two drugs attached to a single ruthenium photocage. This strategy may result in increased photocytotoxicity compared to traditional PACT compounds that release only a single active agent. Secondly, constructing the linkage of two bioactive components in a single PACT prodrug ensures that both components of the combination therapy would reach the tumor in an equimolar ratio at the target location. Last but not least, the photochemical properties of a ruthenium–based prodrug can be tuned in a way that allows for selective release of one component before releasing the second one using specific excitation wavelengths. Such wavelength-dependent behavior may afford favorable treatment options if sequential release of the two components in time would be advantageous.

In Chapter 3, the sequential photosubstitution was reported of two biologically benign compounds pyridine (Py) and methyl(2-thioethanol) (MTE) from *trans* tetrapyridyl-ruthenium complex [Ru(MeL)(Py)(MTE)]$(PF_6)_2$ (MeL = di([2,2'-bipyrid]-6-yl)-N-methylamine). To further explore the applicability of such a photoreactive system for PACT, the incorporation of two biologically active photolabile ligands based on pyridine and thioether functionalities into a single ruthenium-based photocage is reported here (Figure 4.1). Specifically, 4-(((4-(tert-butyl)phenyl)sulfonamido)methyl)-N-(pyridin-3-yl)benzamide (STF31) and 6-benzoyl-2-(3-(methylthio)propyl)-5-phenyl-1,7-dihydro-4H-pyrrolo[2,3-d]pyrimidin-4-one (MTI) were employed as *trans* ligands coordinated at the ruthenium center. The rigidin-analogue MTI inhibits tubulin polymerization while STF31 is a known inhibitor of nicotinamide phosphoribosyl transferase (NAMPT) and glucose transporter 1 (GLUT1).[16,17] Of note, both have been photocaged with ruthenium agent for anticancer PACT treatment, but they have never been combined.[15,18,19] In this work, the complexes *trans*-[Ru(MeL)$(STF31)_2$]$(X)_2$ ([**1**]$(X)_2$) and *trans*-[Ru(MeL)$(MTI)_2$]$(X)_2$ ([**2**]$(X)_2$) were first prepared, followed by the synthesis of the dissymmetric *trans*-[Ru(MeL)(STF31)(MTI)]$(X)_2$ ([**3**]$(X)_2$), where X = hexafluorophosphate (PF_6) or chloride (Cl). The photochemical and photobiological properties of these complexes were compared *in vitro* to demonstrate the potential of dual-targeted PACT in cancer treatment.

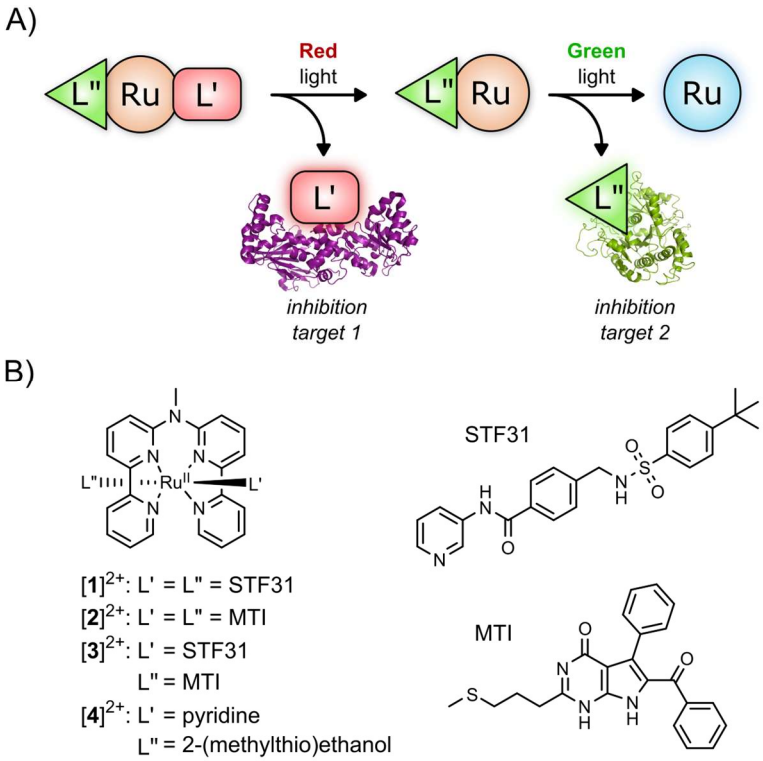

Figure 4.1 A) Schematic overview of multi-targeted photoactivated chemotherapy concept. B) Chemical structures of the compounds presented in this work.

4.2 Results

4.2.1 Synthesis

Following the synthesis of MeL as reported in Chapter 3, the corresponding dichloride-ruthenium precursor **5** was prepared with a good yield through refluxing MeL and [Ru(1,5-cyclooctadiene)Cl_2] in *o*-dichlorobenzene (Figure 4.2). Compounds [**1**]$(PF_6)_2$ and [**2**]$(PF_6)_2$ were synthesized thermally from **5** in presence of an excess of STF31 or MTI, respectively. To ensure dissociation of the coordinated chloride ions in **5**, water (10-20% v/v) was added to the reaction mixture, which facilitated ligand exchange. Compound [**3**](PF_6) was prepared by red-light induced photosubstitution of one of the STF31 ligands in [**1**]$(PF_6)_2$ in presence of 3 molar equivalents of MTI in acetone. The hexafluorophosphate (PF_6) salts of $[\mathbf{1}]^{2+}$ – $[\mathbf{3}]^{2+}$ were finally converted into their corresponding chloride salts by anion exchange chromatography. All compounds were characterized with NMR spectroscopy, mass spectrometry, elemental analysis and UV-Vis spectroscopy (see Appendix IV.4).

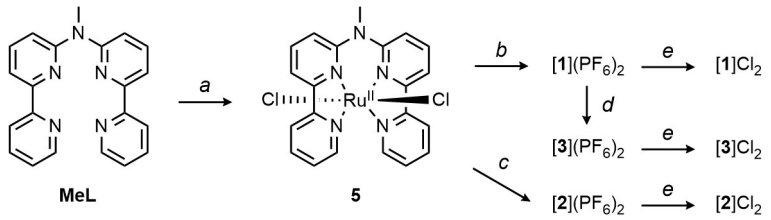

Figure 4.2 Overview of synthetic routes. *a*) [Ru(1,5-cyclooctadiene)Cl_2], *o*-dichlorobenzene, N_2, 180 °C, 48 h, 86%; *b*) i) STF31, methanol with 10% H_2O, 80 °C, 48 h; ii) KPF_6 (sat. aq.), 61%; *c*) i) MTI, ethylene glycol with 20% H_2O, ii) KPF_6 (sat. aq.), 24%; *d*) i) MTI, light irradiation at 650 nm, 1:5 THF:acetone, 25 °C, 1.5 h; ii) KPF_6 (sat. aq.), 28%; *e*) anion exchange resin from PF_6^- to Cl^- in MeOH, ≥95%.

4.2.2 Photochemistry

Since PACT photocages act as prodrugs that only become active upon irradiation, these compounds must first be shown to be stable in absence of light. Therefore, the UV-Vis absorbance spectra of [**1**](PF$_6$)$_2$ – [**3**](PF$_6$)$_2$ in 1:1 H_2O:acetone were monitored in the dark at 298 K. All complexes were found to be thermally stable for at least 12 h (Appendix IV.1.2), and exhibited a metal-to-ligand charge transfer (^{1}MLCT) absorption band between 449 and 489 nm with molar absorptivities between 6500 and 8300 $M^{-1}cm^{-1}$ (Table 4.1 and figure IV.1).

The ^{1}H-NMR spectra of [**1**](PF$_6$)$_2$ – [**3**](PF$_6$)$_2$ in 1:5 D_2O:acetone-*d*$_6$ were monitored upon blue (450 nm), green (530 nm) or red (650 nm) light irradiation to identify the photochemical reactivity of the complexes. For [**1**]$^{2+}$ irradiated with green light (Figure 4.3 A), the doublet at 10.00 ppm corresponding to a C–H signal of the tetrapyridyl ligand was replaced by a doublet at 9.87 ppm within 15 min irradiation. During this period, two doublets at 8.87 and 8.76 ppm appeared corresponding a 1:1 ratio of free STF31 and coordinated STF31, indicating the formation of aqua/STF31 intermediate [**6**]$^{2+}$. After 180 min of green light irradiation, the doublets at 8.76 and 9.87 ppm were replaced by a broad peak at 9.95 ppm while the signals for free STF31 increased further. Similar results were obtained when a solution containing [**2**]$^{2+}$ was irradiated with green light (Figure IV.9), showing the release of MTI with the temporary presence of aqua/MTI intermediate [**7**]$^{2+}$. When a solution [**3**]$^{2+}$ was irradiated with red light, a shoulder peak adjacent to the doublet at 9.89 ppm and a doublet at 9.72 ppm appeared (Figure 4.3 B). In addition, a doublet at 8.87 ppm and multiplet at 7.16 ppm appeared, corresponding to free STF31 and MTI in a ratio around 72:28 after 510 min of red light irradiation. At this time point the other peaks can be assigned to the same intermediates [**6**]$^{2+}$ and [**7**]$^{2+}$ observed during photoreactions of [**1**]$^{2+}$ and [**2**]$^{2+}$. For example, the doublet at 8.76 ppm corresponds to the aqua/STF31 intermediate [**6**]$^{2+}$ and the doublet at 8.64 ppm corresponds to the aqua/MTI intermediate [**7**]$^{2+}$. After irradiation with red light, the solution of [**3**]$^{2+}$ was irradiated with blue light, which resulted in increased intensities of the signals corresponding to free STF31 and free MTI, together with the appearance of broad signals for the final ruthenium bis-aqua

photoproduct [**8**]$^{2+}$ (for example at 9.95 ppm). The integrals of the free STF31 and free MTI peaks revealed, after blue light irradiation for 180 min, a 1:1 ratio between both photoreleased inhibitors. According to these results, red light irradiation released primarily STF31, while further blue light irradiation released the remaining STF31 as well as all MTI ligands.

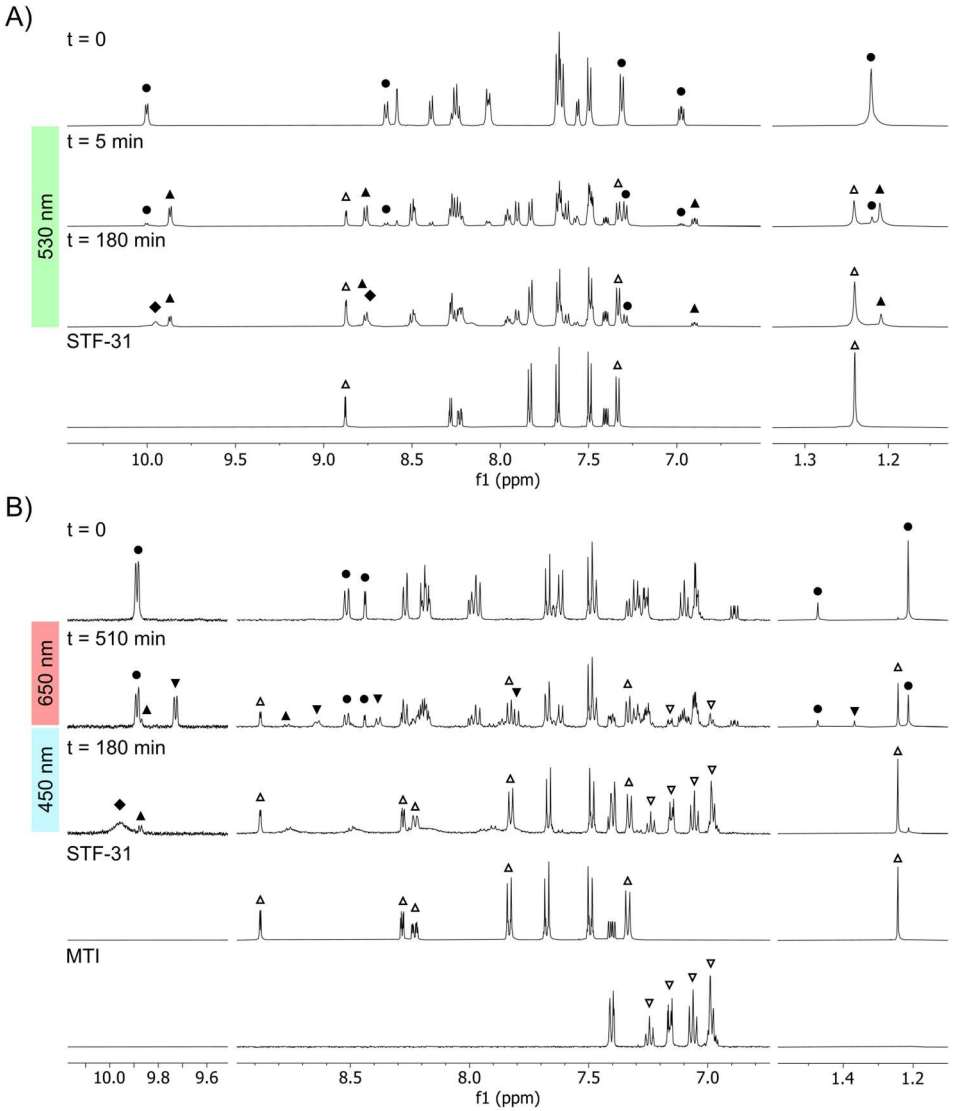

Figure 4.3 Time-evolution of the ^{1}H-NMR spectra of [**1**]$(PF_6)_2$ upon irradiation with green light (180 min) (A) and [**3**]$(PF_6)_2$ irradiated first with red light (510 min) followed by blue light (180 min) (B). Spectra were measured in 1:5 D_2O:acetone-d_6 at 298K. Symbols indicate starting compound (●), intermediates [**6**]$^{2+}$ (▲) or [**7**]$^{2+}$ (▼), STF-31 (△), MTI (▽) or photoproduct [**8**]$^{2+}$ (◆).

As observed during the light irradiated NMR experiments, the reaction from $[\mathbf{1}]^{2+}$ – $[\mathbf{3}]^{2+}$ to bis-aqua photoproduct $[\mathbf{8}]^{2+}$ occurs through a sequential two-step photosubstitution route *via* the formation of a mono-aqua intermediate (Figure 4.4). In the case of $[\mathbf{1}]^{2+}$ and $[\mathbf{2}]^{2+}$, with identical axial ligands, the photoreaction proceeds *via* a single intermediate ($[\mathbf{6}]^{2+}$ for $[\mathbf{1}]^{2+}$, $[\mathbf{7}]^{2+}$ for $[\mathbf{2}]^{2+}$). For complex $[\mathbf{3}]^{2+}$, however, the different axial ligands result in the possible formation of both intermediates $[\mathbf{6}]^{2+}$ or $[\mathbf{7}]^{2+}$ depending on which ligand is initially photosubstituted (Figure 4.4). As photosubstitution of the second ligand in either of the intermediates yields product $[\mathbf{8}]^{2+}$, the overall two-step photoreaction of the dissymmetric complex occurred through a parallel pathways involving four different photosubstitution reactions.

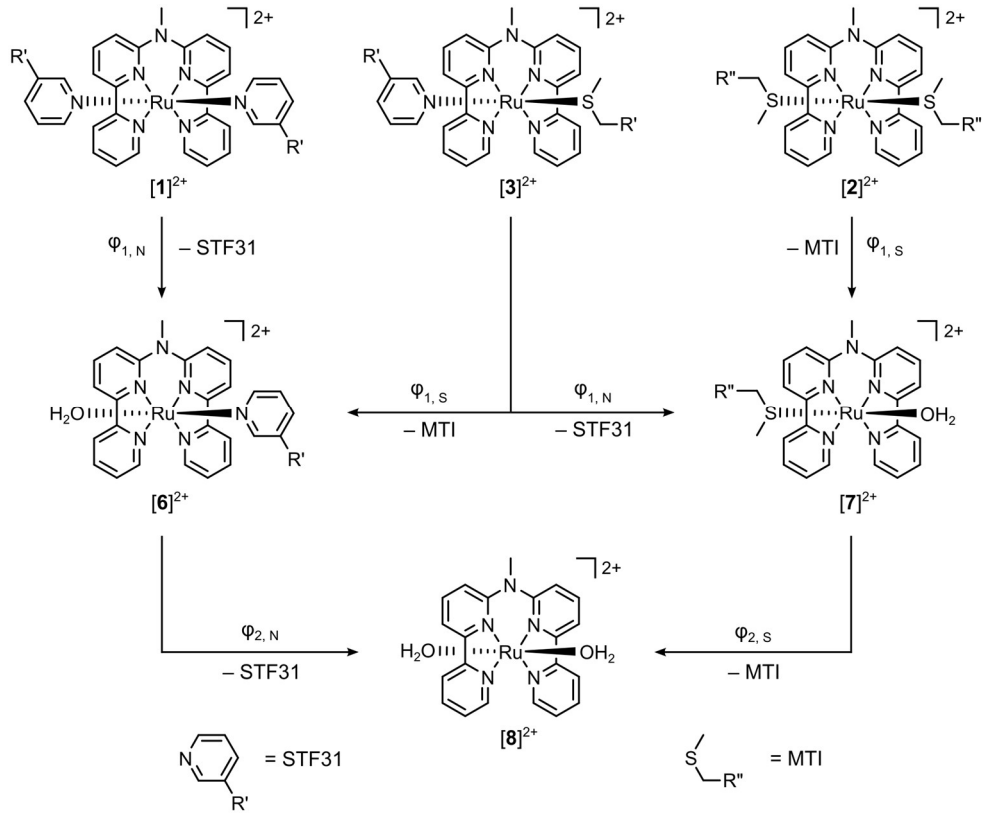

Figure 4.4 Schematic overview of the four possible photosubstitution pathways when irradiating $[\mathbf{1}]^{2+}$ – $[\mathbf{3}]^{2+}$ in H_2O depending on the symmetry of the complex. In the case of a symmetric complexes (i.e. $[\mathbf{1}]^{2+}$ or $[\mathbf{2}]^{2+}$), the photosubstitution of the axial ligands will proceed through a two-step sequential mechanism with specific quantum yields $\phi_{1,X}$ and $\phi_{2,X}$ (X = N for STF31 and X = S for MTI), resulting in bis-aqua product $[\mathbf{8}]^{2+}$. For complex $[\mathbf{3}]^{2+}$, both intermediates $[\mathbf{6}]^{2+}$ and $[\mathbf{7}]^{2+}$ can be formed depending which ligand is photosubstituted first. The resulting two parallel 2-step mechanisms also yield $[\mathbf{8}]^{2+}$.

To further investigate the photosubstitution kinetics, the UV-Vis absorbance spectra of [**1**](PF$_6$)$_2$ – [**3**](PF$_6$)$_2$ in 1:1 acetone:H$_2$O were recorded during irradiation with blue (435 nm), green (505 nm) or red light (625 nm), which are shown in Figure 4.5 and Appendix IV.1.2. The reaction profiles of [**1**]$^{2+}$ and [**2**]$^{2+}$ (insets in Figure 4.5) were obtained *via* global fitting of the kinetic data using *R* package TIMP with Glotaran, which also provided the absorbance spectra of intermediates [**6**]$^{2+}$ and [**7**]$^{2+}$.[20] The spectra of [**6**]$^{2+}$ and [**7**]$^{2+}$ where then used for targeted fitting of the kinetic data of [**3**]$^{2+}$. This methodology provided the necessary information to calculate the photosubstitution quantum yield of all reactions involved in both the two-step sequential mechanisms for [**1**]$^{2+}$ – [**2**]$^{2+}$ and the two parallel two-step mechanisms for [**3**]$^{2+}$. The photosubstitution quantum yields were calculated and are reported in Table 4.1.

The pyridine-bound complexes [**1**]$^{2+}$ and [**3**]$^{2+}$ respond to red light in spite of their low absorbance at 625 nm (molar absorptivity $\varepsilon_{1,625}$ = 3.2 and 120 M^{-1} cm^{-1}, respectively), but the UV-Vis absorbance of a solution of the bis-thioether compound did not change upon red light irradiation (Figure 4.5 D). All compounds showed photoreactivity upon blue or green light irradiation (see Appendix IV.1.2 for time-evolution absorbance spectra upon blue light irradiation), with kinetics that corresponded to a two-step reaction: a fast initial ligand exchange yield a mono-aqua intermediate ([**6**]$^{2+}$ and/or [**7**]$^{2+}$) followed by a second, slower process forming photoproduct [**8**]$^{2+}$. Their data were well-fitted using a sequential model as proposed in Figure 4.4. For all complexes, the photosubstitution quantum yields of the first step (φ_1) were found to be 2 to 3 orders of magnitude higher than those of the second step (φ_2). While for bis-thioether complex [**2**]$^{2+}$ $\varphi_{1,S}$ and $\varphi_{2,S}$ were nearly identical upon blue or green light irradiation (~0.013 for $\varphi_{1,S}$ and ~0.00006 for $\varphi_{2,S}$), no significant photosubstitution was observed when red light was used ($\varphi_{1,S} < 0.00010$ and $\varphi_{2,S} < 0.00001$). However, the photosubstitution quantum efficiencies for the bis-pyridine complex [**1**]$^{2+}$ were similar when irradiated with blue, green or red light, both for the first ($\varphi_{1,N}$ values of 0.012, 0.0078 and 0.014, respectively) and second photosubstitution ($\varphi_{2,N}$ values of 0.00007, 0.00007 and 0.00010, respectively). In a way, this complex seemed to obey Kasha–Vavilov rule, stating that the outcome of a photoreaction is independent of irradiation wavelength.[21] By contrast, for the dissymmetric complex [**3**]$^{2+}$ the photosubstitution quantum yields were dependent on irradiation wavelength. Especially the ratio between $\varphi_{1,S}$:$\varphi_{1,N}$ ($\varphi_{1,S}$ relates to MTI substitution and $\varphi_{1,N}$ to STF31 substitution) deviated strongly when irradiated with blue ($\varphi_{1,S}$:$\varphi_{1,N}$ = 0.0042:0.012 = 0.35), green ($\varphi_{1,S}$:$\varphi_{1,N}$ = 0.0017:0.015 = 0.11) or red light ($\varphi_{1,S}$:$\varphi_{1,N}$ = 0.00005:0.00029 = 0.17). The higher quantum yields observed for STF31 photosubstitution compared to MTI from [**3**]$^{2+}$, suggested that the excited states leading to the dissociation of STF31 were populated more efficiently under certain excitation wavelengths. Quenching of the excited state by oxygen

seems to be insignificant, as no singlet oxygen generation was observed for [**1**](PF$_6$)$_2$ – [**3**](PF$_6$)$_2$, with quantum yields (φ_Δ) of <0.01 in acetonitrile.

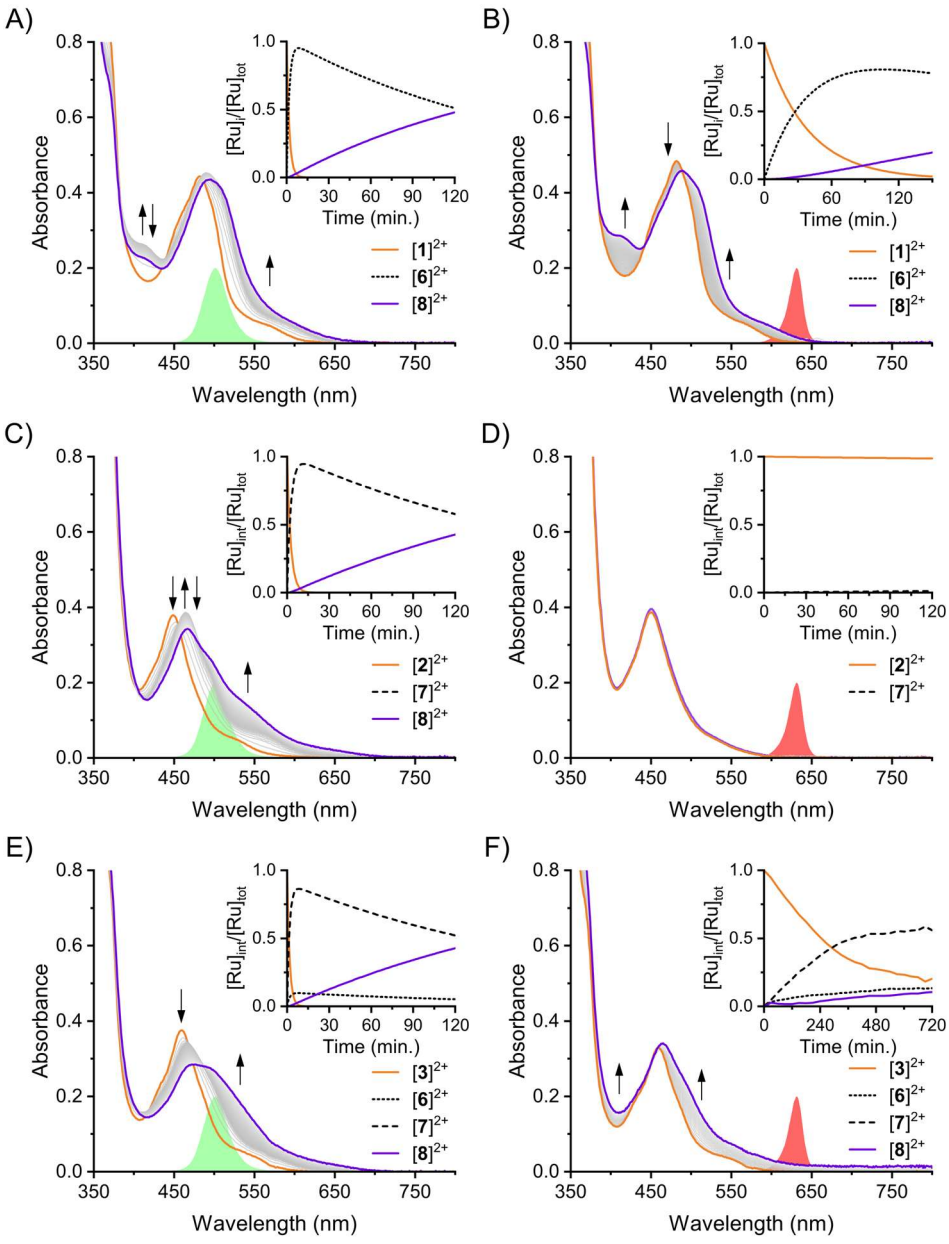

Figure 4.5 Time-evolution of the UV-Vis absorbance spectra of [**1**](PF$_6$)$_2$ at 59 µM (A, B), [**2**](PF$_6$)$_2$ at 61 µM (C, D) and [**3**](PF$_6$)$_2$ at 56 µM (E, F) in 1:1 acetone/H_2O at 298 K upon irradiation with green light (A, C, E; 505 nm, photon flux = 2.27 × 10^{-7} mol.s^{-1}) or red light (B, D, F; 625 nm, photon flux = 4.32 × 10^{-7} mol.s^{-1}). Arrows indicate changes in the spectra (from orange to purple). Inserts depict the time-

evolution of the fraction of starting reactant (orange line), intermediates (dotted black line for $[\mathbf{6}]^{2+}$, dashed black line for $[\mathbf{7}]^{2+}$) or photoproduct $[\mathbf{8}]^{2+}$ (purple line).

Table 4.1 Photochemical properties of $[\mathbf{1}](PF_6)_2$, $[\mathbf{2}](PF_6)_2$ and $[\mathbf{3}](PF_6)_2$ in 1:1 acetone:H_2O at 298 K including maximum absorption wavelength (λ_{max}, in nm), molar absorptivity (ε_{max}, in $M^{-1}cm^{-1}$), photosubstitution quantum yield (φ_i) for each step with the corresponding photosubstitution reactivity (ζ_i) and molar absorptivity at the irradiation wavelength (ε_i) and singlet oxygen generation quantum yield (φ_Δ).[a]

		$[\mathbf{1}]^{2+}$	$[\mathbf{2}]^{2+}$	$[\mathbf{3}]^{2+}$	
	λ_{max} (nm) (ε_{max})[b]	484 (8300)	449 (6500)	459 (6500)	
		$\varphi_{i,N}$	$\varphi_{i,S}$	$\varphi_{i,N}$	$\varphi_{i,S}$
435 nm	ε_1[b]	2600	5100	4100	4100
	φ_1	0.012[d]	0.013[e]	0.012[d]	0.0042[e]
	(ζ_1)	(32)	(69)	(49)	(18)
	ε_2[c]	4000	5100	4000	5100
	φ_2	0.00007[f]	0.00004[g]	0.00031[f]	0.00006[g]
	(ζ_2)	(0.26)	(0.21)	(1.2)	(0.23)
505 nm	ε_1[b]	5500	1200	1700	1700
	φ_1	0.0078[d]	0.014[e]	0.015[d]	0.0017[e]
	(ζ_1)	(43)	(18)	(25)	(2.8)
	ε_2[c]	7300	3700	7300	3700
	φ_2	0.00007[f]	0.00008[g]	0.00044[f]	0.00009[g]
	(ζ_2)	(0.55)	(0.28)	(1.6)	(0.66)
625 nm	ε_1[b]	3.2	20	120	120
	φ_1	0.014[d]	<0.00010[e]	0.00029[d]	0.00005[e]
	(ζ_1)	(0.46)	(<0.0020)	(0.034)	(0.0063)
	ε_2[c]	360	260	360	260
	φ_2	0.00010[f]	<0.00001[g]	0.00007[f]	0.00002[g]
	(ζ_2)	(0.035)	(<0.0026)	(0.025)	(0.0052)
	φ_Δ[h]	<0.01	<0.01	<0.01	

[a] $\zeta_i = \varepsilon_i \times \varphi_i$. [b] Molar extinction coefficient determined experimentally. [c] Molar extinction coefficient determined by global fitting. [d] Quantum yield ($\varphi_{1,N}$) and photoreactivity ($\zeta_{1,N}$). [e] Quantum yield ($\varphi_{1,S}$) and photoreactivity ($\zeta_{1,S}$). [f] Quantum yield ($\varphi_{2,N}$) and photoreactivity ($\zeta_{2,N}$). [g] Quantum yield ($\varphi_{2,S}$) and photoreactivity ($\zeta_{2,S}$). [h] determined by $^1O_2$ phosphorescence (λ_{em} = 1275 nm) in aerated acetonitrile at 298 K. Excitation wavelength (λ_{irr}) = 450 nm.

As revealed by the kinetic modeling of the UV-Vis data upon red-light irradiation of [**3**]$^{2+}$, the initial photosubstitution reaction primarily led to the formation of MTI-bound intermediate [**7**]$^{2+}$ (Figure 4.5 F). Importantly, the difference in quantum yields for the formation of STF31-bound [**6**]$^{2+}$ (photosubstitution of MTI) and MTI-bound [**7**]$^{2+}$ (photosubstitution of STF31) was dependent on the excitation wavelength (Table 4.1). For red light, the quantum yield for the formation of towards [**7**]$^{2+}$ ($\phi_{1,N}$) was six times higher than for the formation of [**6**]$^{2+}$ ($\phi_{1,S}$). It was therefore hypothesized that it may be possible to sequentially release STF31 first, and MTI second, by subsequent irradiation with red and blue light. Indeed, as shown in Figure 4.3 B, the ^{1}H-NMR irradiation experiment for [**3**]$^{2+}$ (1.38×10^{-3} M) in 5:1 acetone-D_6:D_2O demonstrated the selective release of the two inhibitors after first using red light (650 nm), followed by blue light (450 nm). After identification of the ^{1}H-NMR signals of free STF31 (8.9 ppm) and free MTI (7.0 ppm), the relative concentrations of the released inhibitor was determined by calculating the integral ratios, which demonstrate sequential release (Figure 4.6 A). To further investigate sequential release of the axial ligand, a similar irradiation experiment (first 625 nm, then 435 nm light) was conducted while monitoring the UV-Vis absorbance of a solution of [**3**]$^{2+}$ (5.62×10^{-7} M) in 1:1 H_2O:acetone. Targeted fitting of the time-evolution UV-Vis absorbance spectra provided relative concentrations of the ruthenium-based components during the photoreaction (Figure 4.6 B). During the first irradiation step in the UV-Vis setup, [**3**]$^{2+}$ was mainly converted into [**7**]$^{2+}$ (releasing STF31) with red light while the second irradiation step resulted in the formation of [**8**]$^{2+}$. Although the conditions of the NMR and UV-Vis experiments differ in solvent, light sources, concentration of [**3**]$^{2+}$ and overall irradiation setup, the results of both experiments indicated selective photosubstitution of STF31 upon red light irradiation, followed by complete release of the inhibitors and the formation of [**8**]$^{2+}$ upon blue light irradiation. These results highlight the robustness of the sequential photosubstitution reaction from [**3**]$^{2+}$ and exceptional wavelength-dependent control of photorelease.

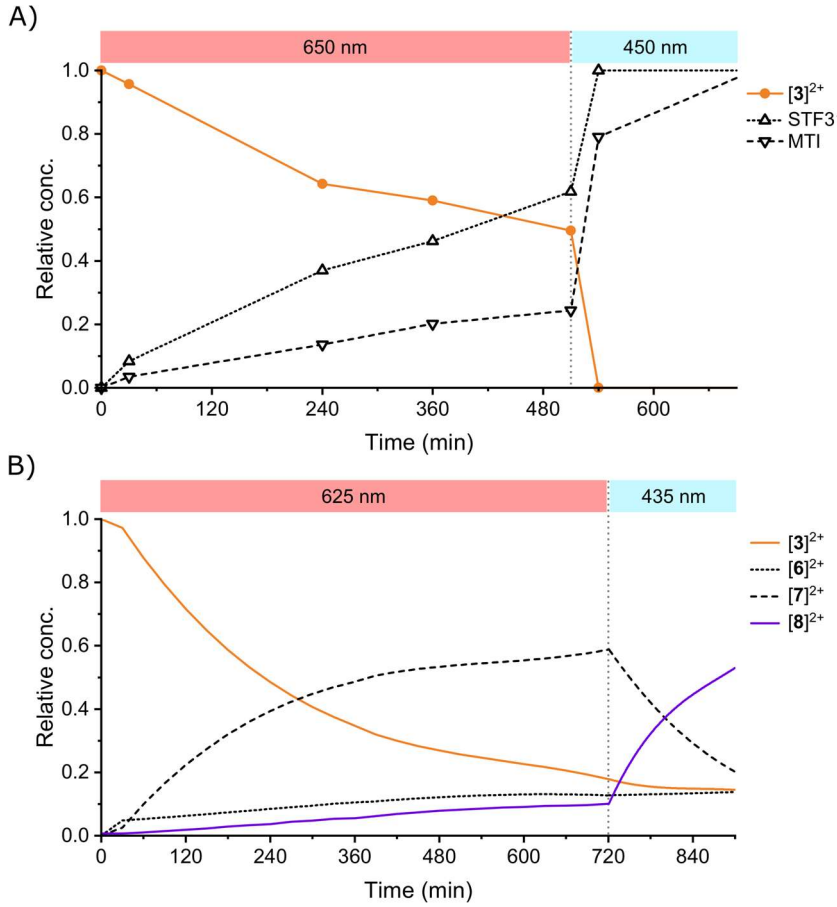

Figure 4.6 Sequential release of STF-31 and MTI from [**3**](PF$_6$)$_2$ upon irradiation with red light followed by blue light. A) Relative concentration profile of [**3**]$^{2+}$, STF-31 and MTI followed by ^{1}H-NMR upon irradiation with 650 nm (t = 0 – 510 min) followed by 450 nm (t = 510 – 690 min) at 298 K. Starting concentration of [**3**]$^{2+}$ = 1.38 × 10^{-3} M in 5:1 acetone-D6:D$_2$O. The relative concentration profile was derived from the integral ratios (9.9 ppm for [**3**]$^{2+}$; 8.9 ppm for STF31; 7.0 ppm for MTI). B) Relative concentration profile of [**3**]$^{2+}$, [**6**]$^{2+}$, [**7**]$^{2+}$ and [**8**]$^{2+}$ followed by UV-Vis absorbance upon irradiation with 625 nm (t = 0 – 720 min; photon flux = 4.32 × 10^{-7} mol.s^{-1}) followed by 435 nm (t = 720 – 900 min; photon flux = 2.27 × 10^{-7} mol.s^{-1}) at 298 K. Starting concentration of [**3**]$^{2+}$ = 5.62 × 10^{-7} M in 1:1 acetone:H$_2$O. Relative concentration profile was derived from the time-evolution of the UV-Vis spectrum of the solution for which the method described in Appendix I.2.3 (Equation I.8).

4.2.3 Cytotoxicity and cellular uptake

Considering the well-characterized photoreactivity of all three complexes under different irradiation conditions, we investigated the consequence of these photoreactions *in vitro*. As [**3**]$^{2+}$ can photorelease STF31 and MTI in a 1:1 ratio upon full activation, the cytotoxicity of the ruthenium PACT compounds [**1**]Cl$_2$ – [**3**]Cl$_2$ was evaluated together with that of a 1:1 combination of free STF31 and free MTI. All *in vitro* experiments were realized under

normoxic (21% O_2) and hypoxic conditions (1% O_2) in human skin melanoma (A375), lung (A549) and glioblastoma (U87MG and U251) cancer cell lines. The dissymmetric ruthenium compound [Ru(MeL)(Py)(MTE)]Cl_2 ([**4**]Cl_2, see Chapter 3) was added to this study to investigate the effect of only the ruthenium cage in the same conditions, assuming that free pyridine and free MTE had negligible biological effects. In all cases, the chloride salts of the compounds were used, because of their increased solubility in aqueous solution. To evaluate the light dose needed to ensure full activation in the cell irradiation setup, a mock irradiation experiment was realized for both wavelengths used in this study (see Appendix IV.1.5). The necessary light doses were 30.8 J/cm^2 for green light (520 nm) and 115 J/cm^2 for red light (630 nm; Figure IV.10). The cytotoxicity of the compounds was then determined as described in Appendix I.3. In short: the different cell lines were treated with either prodrug or the 1:1 free drug mixture and incubated in the dark for 24 h. The medium was then replaced by drug-free medium, and the cells were irradiated with green light (530 nm, 30.8 J/cm^2), red light (630 nm, 115 J/cm^2), or kept in the dark. The cells were further incubated in the dark for 48 h, and at t = 96 h the cell viability assessed using the MTT metabolic activity assay and compared to the untreated control. From the resulting dose-response curves, the metabolic activity inhibition effective concentrations (EC_{50} in µM) were determined (Figure 4.7 and Tables IV.2, IV.3).

For all cell lines, the ruthenium cage [**4**]Cl_2 was found to be non-cytotoxic (EC_{50} > 100 µM) both in the dark and after light irradiation (Table IV.2). Therefore, no cytotoxic effect originating from the ruthenium cage (or pyridine or MTE) is expected. On the other hand, the free inhibitors did induce a significant effect on cell proliferation: STF31 was highly cytotoxic for A375, A549 and U251 (EC_{50} < 5 µM), but less for U87MG (EC_{50} > 18 µM). Additionally, STF31 appeared to be more potent under normoxia than in hypoxia. This result is possibly related to upregulation of NAMPT expression induced by hypoxia-inducible factor 1α (HIF1α).[22] The microtubule inhibitor MTI showed a similar cytotoxic effect on all cell lines (EC_{50} < 7 µM), although with some contrasting differences. In A375, MTI was found to be almost eight times more cytotoxic under normoxia than in hypoxia (EC_{50} = 0.26 µM *vs.* 1.97 µM respectively), while the reverse was observed in A549 (EC_{50} = 6.21 µM *vs.* 0.91 µM respectively). Furthermore, the 1:1 combination of STF31 and MTI was shown to be highly cytotoxic to all cell lines (EC_{50} < 1.3 µM). Strikingly, cotreatment with STF31 and MTI was found to be more cytotoxic in all cell lines, except in A375 cells under normoxia, compared to treatment with one of the drugs. These results suggest a potential synergistic effect of MTI and STF-31 on the reduction of cell viability, independent of oxygen concentration.

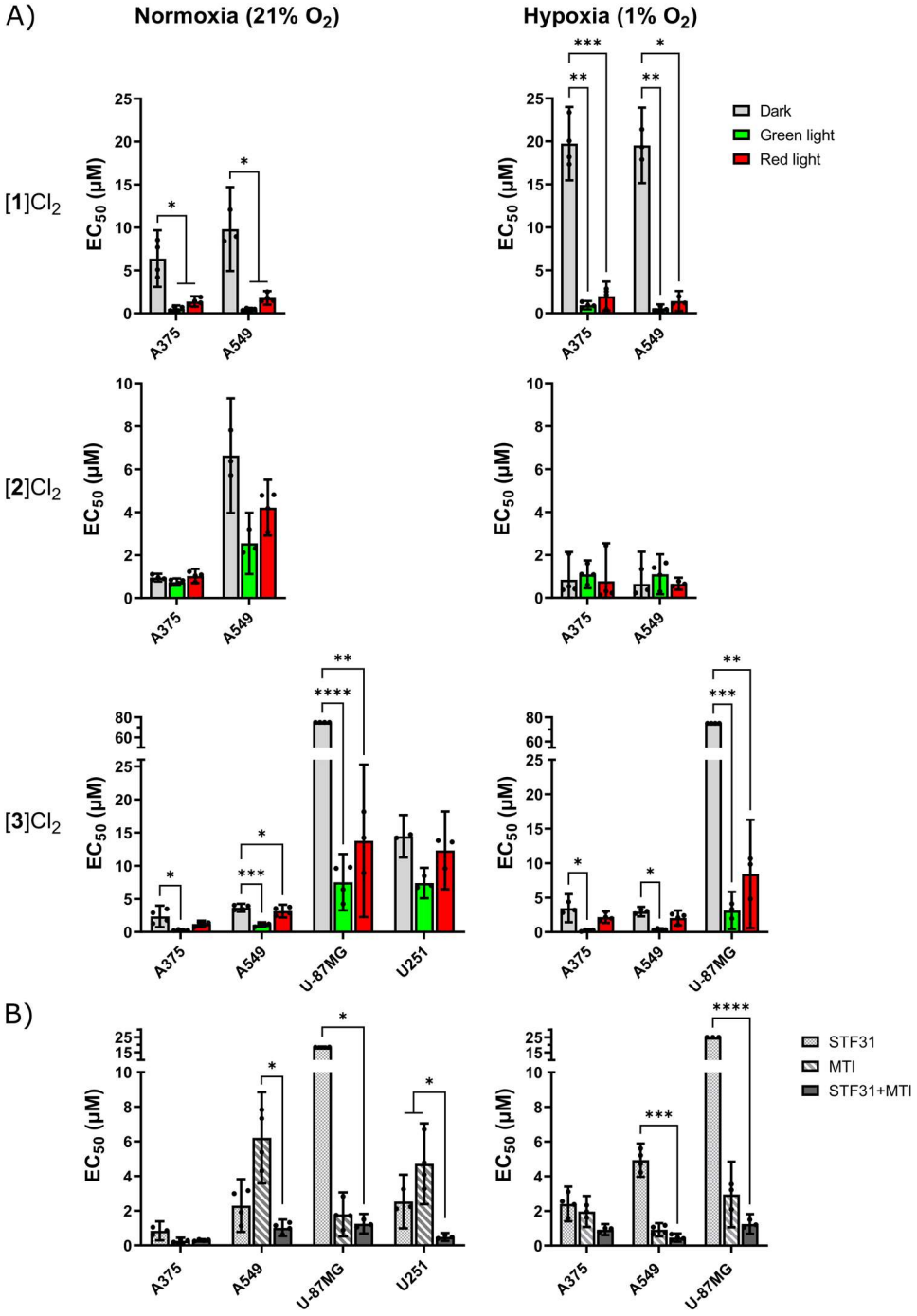

Figure 4.7 Metabolic activity inhibition effective concentrations (EC_{50} in μM) in A375, A549, U87MG and U251 human cancer cell lines incubated in normoxic (21% O_2) or hypoxic (1% O_2) conditions. A) EC_{50} for [**1**]Cl_2, [**2**]Cl_2 and [**3**]Cl_2 in the dark and upon irradiation with green light (520 nm, 30.8

J/cm²) and red light (630 nm, 115 J/cm²). B) EC_{50} for STF31, MTI and STF31 + MTI (1:1 molar ratio). Experiments were performed in biological quadruplicate; error bars indicate 95% confidence intervals (in µM). * = p ≤ 0.05, ** = p ≤ 0.01, *** = p ≤ 0.001, **** = p ≤ 0.0001, ns = Not Significant has been omitted for clarity. See Table IV.1 and IV.2 for all EC_{50} values.

The symmetric ruthenium-caged MTI-releasing compound [**2**]Cl_2 showed high cytotoxicity, comparable to free MTI, in both A375 and A549 cells under normoxic and hypoxic conditions ($EC_{50,\ dark}$ < 7 µM). However, no significant differences were observed between irradiated and non-irradiated cells, suggesting thermal release of the MTI inhibitor in cell media. This result was in great contrast to those obtained with the symmetric STF31-releasing compound [**1**]Cl_2, which was much less cytotoxic in the dark and in normoxia in A375 and A549 cell lines, and became far more cytotoxic after irradiation with both red and green light (EC_{50} < 2 µM and < 0.6 µM, respectively). Under hypoxia, the photoactivation of [**1**]Cl_2 had even stronger effects, characterized by a lower dark toxicity ($EC_{50,\ dark}$ > 19 µM) while maintaining a similar cytotoxicity after irradiation, compared to normoxic conditions. This resulted in an increase of the photoindices under hypoxia for [**1**]Cl_2 with both red light and green light. For red light, the PI values went from 4.6 and 5.5 for A375 and A549 cells under normoxia to 10 and 14 under hypoxia, respectively. For green light, they increased from 12 and 22 for A375 and A549 under normoxia to 21 and 33 under hypoxia, respectively. As note, these PI values were considerably higher than the ones found for the previously reported ruthenium-caged STF-31 compound [Ru(tpy)(biq)(STF-31)]Cl_2 (tpy = 2,2';6',2"-terpyridine, biq = 2,2'-bisisoquinoline) which were 2.6 and 2.4 for A549 cells in normoxia and hypoxia, respectively.[19] It is unclear at this stage if these much improved PI values for [**1**]Cl_2 are due to the double amount of STF-31 molecules released by the ruthenium cage, to the different nature of the ruthenium cage, to the different lipophilicity and/or cellular localization of the caged prodrug, or to several of these factors at the same time.

For the dissymmetric compound [**3**]Cl_2, a relatively high toxicity was found in the dark ($EC_{50,\ dark}$ < 4 µM) across both A375 and A549 cell lines under normoxic and hypoxic conditions. Nonetheless, green light activation resulted in a significantly increased cytotoxicity ($EC_{50,\ 520nm}$ < 1 µM). It should be noted that like for [**1**]Cl_2 the green light-induced photoindexes in A375 and A549 cells under hypoxia increased two-fold compared to normoxia (8.7 and 3.3 under normoxia, and 16 and 8.1 under hypoxia, respectively). The sensitivity of the U87MG and U251 cells towards [**3**]Cl_2 differed notably despite both being glioblastoma cell lines. In U251 cells, [**3**]Cl_2 exhibited measurable dark cytotoxicity under normoxic conditions (($EC_{50,\ dark}$ = 14 µM). In contrast, no dark toxicity was detected in U87MG cells ($EC_{50,\ dark}$ > 75 µM), either in normoxic or hypoxic conditions. Upon irradiation with green or red light, no significant change was observed for [**3**]Cl_2 in U251 cells. By comparison, pronounced phototoxicity was observed in U87MG cells under normoxia, with EC_{50} values of 7.51 µM under green light (PI > 10) and 13.8 µM under red light (PI > 5.5). This light-induced cytotoxicity was further enhanced under hypoxic conditions, yielding EC_{50} values of 3.13 µM

under green light (PI > 24) and 8.44 μM under red light (PI > 9). Notably, this behavior is unusual, as most ruthenium-based PACT compounds reported up to now exhibit either similar or strongly reduced photoindices under hypoxia relative to normoxia.

To investigate the potential synergistic effect exerted by STF31 and MTI in the 1:1 mixture or for the green light-activated complex [**3**]$^{2+}$, the CompuSyn software was used to calculate the combination indexes (CI) based on the Chou-Talalay method (see experimental section 4.5 for details).[23] With this method, CI values are determined for each drug combination as a function of the fraction of affected cells (F_a), thereby allowing evaluation of drug interactions across different effect levels. The CI values can be used to define the nature of the combination effect: an additive effect is indicated by CI = 1, synergism by CI < 1, and antagonism by CI > 1. In Figure 4.7, the Chou-Talalay plots are shown for treatment of A375, A549, U87MG and U251 in normoxia or hypoxia with 1:1 STF31:MTI or green light-activated [**3**]$^{2+}$ at a light dose where it is fully activated and has released both inhibitors.

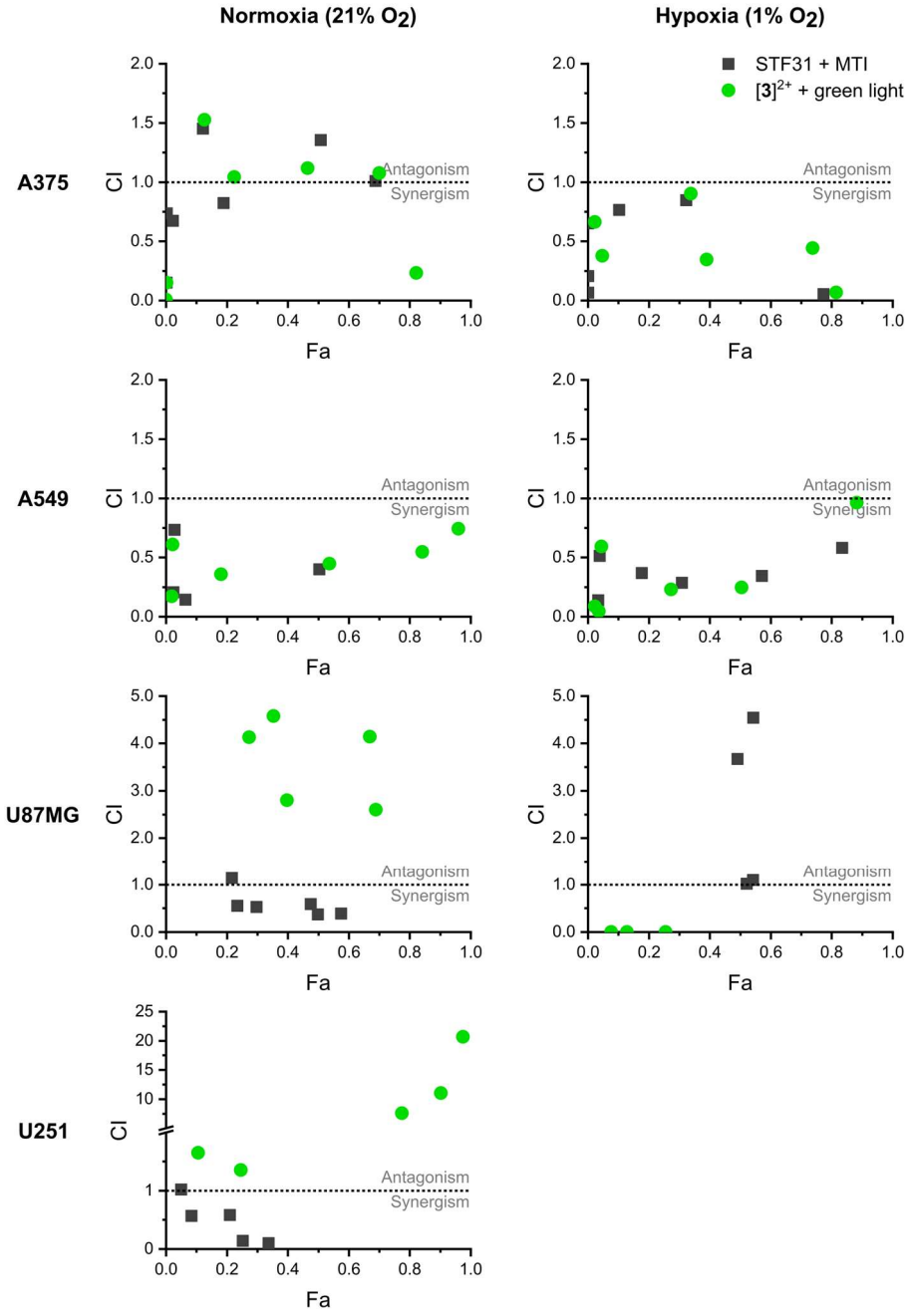

Figure 4.7 Chou-Talalay plots for combination treatment with STF31:MTI mixtures (1:1 molar ratio; grey squares), or [**3**]$^{2+}$ after green light activation (green circles) in A375, A549, U87MG and U251 under normoxic (21% O_2) or hypoxia (1% O_2). The y-axis indicates the combination index (CI) at an observed effect upon treatment generating an effect F_a on the x-axis.

For the A375 and A549 cells, the data points for both STF31:MTI and photoactivated [**3**]$^{2+}$ were comparable, pointing to similar CI values, indicating that the effect of co-treatment with a 1:1 mixture of both free drugs was retained when both inhibitors were released by green light activation of [**3**]$^{2+}$. For A375 cells in normoxia, the data points were spread around CI = 1, suggesting an additive effect. However, CI values clearly below 1 were observed in hypoxic cells, indicative for synergy in such conditions. The CI values were all well-below 1 in A549 cells in both normoxia and hypoxia, indicating a strong synergistic effect independent of the oxygen concentration for these cells. In glioblastoma cells, larger differences between the CI values of STF31:MTI and photoactivated [**3**]$^{2+}$ were observed. While synergy was observed for STF31:MTI mixtures in normoxic U87MG cells, photo-releasing these inhibitors from [**3**]$^{2+}$ resulted in an antagonistic effect in the same conditions. These differences were more pronounced in U251 cells. Strikingly, however, in hypoxic U87MG cells this difference was completely reversed, leading to strong synergism for light-activated [**3**]$^{2+}$ while the combined mixture of free inhibitors worked antagonistically. Although only speculations can be made at this stage, these contrasting results between the photo-released mixture and the combination of free inhibitors in the glioblastoma cell lines may be related to differences in cellular uptake mechanisms and/or intracellular localization. Further studies will be needed to investigate the cell line-dependent effects on the drug-drug interactions and may provide be a better understanding of the cellular pathways that are involved upon the combined inhibition of tubulin polymerization and NAMPT inhibition.

Cellular uptake has a crucial influence on the therapeutic efficacy of a drug, and it is expected to play an important role on the efficacy of ruthenium-based PACT prodrugs as well. Therefore, the intracellular ruthenium content of A375, U87MG and U251 cells incubated with [**1**]Cl_2 – [**3**]Cl_2 in the dark and under normoxia or hypoxia for 24 h was quantified by ICPMS. This uptake was compared to the molar amount of added compound, to investigate potential differences in cellular accumulation of the three compounds. To ensure a number of live cells sufficient for analysis, the compounds were incubated at concentrations below their EC_{50} (see Figure 4.8 for details). As note, comparison of these results can therefore only be done qualitatively as different concentrations were used for the different compounds. As shown in Figure 4.8 A, the ruthenium uptake efficiency in A375 cells after incubation with [**1**]Cl_2 was thrice lower in hypoxia compared to normoxia (6% *vs.* 19%, respectively). This result indicates a significant effect of the oxygen concentration on the accumulation of [**1**]$^{2+}$ and suggest potentially reduced efficacy against hypoxic tumors. In contrast, incubation with [**2**]$^{2+}$ resulted in minimal uptake (<1.5%) regardless of the oxygen concentration. Accumulation of [**3**]$^{2+}$ was observed in A375 independent from oxygen concentration, with uptake efficiencies of 2.7% in normoxia and 2.5% in hypoxia (Figure 4.8 B). Furthermore, in normoxia the uptake of [**3**]$^{2+}$ was found to be more efficient by the U87MG and U251 glioblastoma cells (8% and 11%, respectively). In hypoxia, uptake

of [**3**]$^{2+}$ by U87MG was similarly efficient as in normoxia (7% and 8%, respectively). While slight differences are observed between the different cell lines, the cellular uptake efficiency of [**3**]$^{2+}$ was generally independent of the oxygen concentration. Unfortunately, the uptake of free drugs STF31 and MTI could not be determined with the tools available in our laboratories.

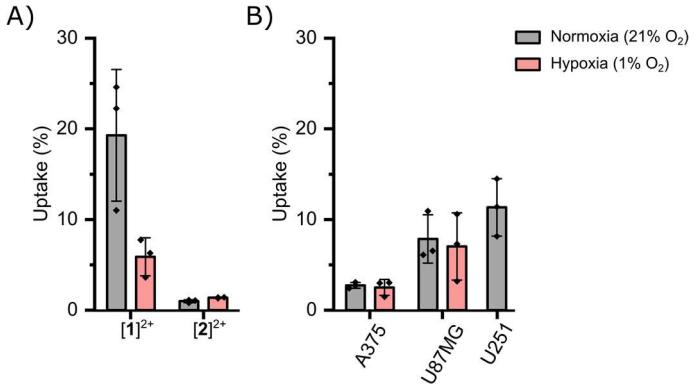

Figure 4.8 Cellular ruthenium uptake efficiency (percentage uptake per million cells of the administered dose) in different human cancer cells under normoxic and hypoxic conditions as determined by ICP-MS. A) Ruthenium uptake of A375 cells incubated with [**1**]Cl_2 (2 µM) or [**2**]Cl_2 (0.5 µM) for 24 h in the dark. B) Ruthenium uptake of A375, U87MG or U251 human cancer cell lines incubated with [**3**]Cl_2 (1 µM for A375, 5 µM for U87MG NX, 10 µM for U87MG HX and U251) for 24 h in the dark. Boxes are the mean of three biologically independent experiments, and error bars depict standard deviation (in µM). See Table IV.4 for exact values.

4.3 Discussion

While the red-light molar absorptivity of the complexes reported here are low (>200 $M^{-1}cm^{-1}$ at 625 nm), only [**2**]$(PF_6)_2$ was not reactive upon irradiation at this wavelength. [**1**]$(PF_6)_2$ and [**3**]$(PF_6)_2$ demonstrate the interesting red-light sensitive photocaging properties of the new [Ru(MeL)$(L)_2]^{2+}$ scaffold. Furthermore, the photosubstitution quantum yields with blue (435 nm) and green (505 nm) light for [**1**]$(PF_6)_2$ and [**2**]$(PF_6)_2$ are within the same order of magnitude (~0.01 for the first step and 0.00006 for the second). Although the available data do not allow for a definitive explanation for the lack of red-light photoreactivity observed for the bis-thioether complex [**2**]$(PF_6)_2$, this behavior is likely related to thermal or emissive relaxation pathways from the excited state.

The quantum yield for STF31 photosubstitution were comparable for [**3**]$^{2+}$ and [**1**]$^{2+}$ upon blue light irradiation (0.012 for both complexes) and remained of the same order of magnitude under green light (0.015 for [**3**]$^{2+}$ versus 0.0078 for [**1**]$^{2+}$). In contrast, upon red light irradiation, STF31 photosubstitution was significantly more efficient for [**1**]$^{2+}$ than for [**3**]$^{2+}$, with quantum yields of 0.014 and 0.00029, respectively. For MTI, the

photosubstitution reaction occurred significantly less efficient for [**3**]$^{2+}$ than [**2**]$^{2+}$. These results suggest that the thioether-based MTI and the pyridine-based STF31 ligands coordinated in *trans*-position in [**3**]$^{2+}$ affect the photoreactivity of the complex, similar to the excited state *trans*-effects for *trans*-[Ru(MeL)(pyridine)(MTE)]$^{2+}$ discussed in Chapter 3. Nonetheless, the more efficient photoreaction for STF31 substitution compared to MTI from [**3**]$^{2+}$ makes it possible to selectively release STF31 upon red light irradiation.

As demonstrated for [**1**]$^{2+}$, incorporation of two equivalents of the same inhibitors on a PACT complex can increase its overall cytotoxicity and potency. It allows for doubling of the amount of delivered inhibitor, while probably also significantly changing the lipophilicity of the complex. This approach has been pioneered by the Turro group who reported ruthenium cages featuring two or more equivalents of 5-cyanouracil (5CNU) that were released upon white-light activation.[24,25] Yet, the *in vitro* cytotoxicity after irradiation of these compounds did not reach the same level as free 5CNU, making the authors suggest that only a single 5CNU ligand was released in these conditions. This difference with our results highlights the importance of an optimization of the light irradiation conditions in relation to the photoreactivity of a given photocage. On the other hand, the cytotoxic effect of a PACT compound releasing two equivalents of an inhibitor per ruthenium center could be in principle also reached by doubling the dose of a "traditional" PACT compound bearing a single inhibitor per ruthenium center. However, increasing the dose of such a "singular" PACT compound to reach the same effect as a double PACT compound also increase the chance of undesirable side-effects. Nonetheless, if the Ru cage is biologically inactive, the added value of a double PACT compound such as [**1**]$^{2+}$ or [**2**]$^{2+}$ is limited, while the applicability of such compounds for the treatment of various cancer types is not guaranteed and the possibility of drug resistances often observed for monotherapies remains. The phototoxicity of the dissymmetric complex [**3**]$^{2+}$ in the different cell lines reported here clearly demonstrated, however, the advantages of dual-targeting PACT. Even if synergy between the two different photoreleased ligands did not occur in every cancer cell type, the overall effect of the treatment was surprisingly better, compared with the individual monotherapies.[26] Furthermore, releasing two different inhibitors from a single PACT compound (such as [**3**]$^{2+}$) can be advantageous compared to co-treatment with two free inhibitors, or the combination of two PACT compound each releasing one inhibitor. The use of two PACT compounds simultaneously clearly comes with the same spatiotemporal challenge as with mixtures of free chemotherapeutic drugs: both PACT compounds should reach the cells at the same time to be able to generate synergies following simultaneous light activation. Therefore, a single PACT compound releasing two different inhibitors, appears as the more powerful approach.

Even though the synergy between biologically active compounds can be rationalized in some cases, most synergistic effects remain challenging to explain due to the complexity of

cancer cell biology. The synergistic combination of STF31 and MTI investigated here is also difficult to explain rationally, although a number of reports in the literature provide indicative evidence that both inhibitors might act synergistically. A study by Harkcom et al. showed that increasing levels of intracellular NAD^+ blocked the microtubule disassembly by microtubule depolymerizing agents such as colchicine, vinblastine and nocodazole, reducing the cytotoxicity of the drugs.[27] This NAD^+-dependent drug resistance was mediated by the activation of mitochondrial sirtuin-3 (SIRT3), a protein involved in metabolic regulation and mitigation of oxidative stress within the cancer cell. The NAD^+–SIRT3 mediated regulation of microtubule dynamics was observed in multiple human cancer cell lines (MCF-7, HEK293T and HeLa), suggesting a cellular pathway that is conserved between different cancer types. As also suggested by the authors, the combination of a microtubule depolymerizing agent (such as MTI) and an inhibitor of the NAD^+ synthesis (such as NAMPT inhibitor STF31) might lead to a synergistic effect on cancer cell proliferation, which is corroborated by our observations. Besides the synergy between STF31 and MTI observed under normoxia, a stronger cytotoxic effect after photoactivation of $[\mathbf{3}]^{2+}$ was observed in hypoxia compared to normoxia. This O_2-dependent effect was rather unexpected as PACT compounds, and chemotherapeutics in general, usually become less cytotoxic with decreasing oxygen concentration.[28] The persisting synergistic effect between STF31 and MTI photoreleased from $[\mathbf{3}]^{2+}$ at low oxygen concentrations may be related to mitochondrial dysfunction. In hypoxia, perinuclear localization of mitochondria is known to activate of HIF-1α, the main transcription factor responsible for the hypoxia response.[29] This mitochondrial clustering around the nucleus is driven by the dynein motor system, facilitating the retrograde mitochondrial movement along the microtubules. Consequently, inhibition of microtubule polymerization (by inhibitors such as MTI) diminishes perinuclear mitochondrial localization. On the other hand, NAMPT inhibition has been shown to cause mitochondrial dysfunction.[30] Therefore, the combined inhibition of NAMPT and microtubule polymerization might exert negative effects on downstream mechanisms that are crucial for cell survival in hypoxia. With the current available data, this analysis only remains a hypothesis. However, the potency of photoactivated release of STF31 and MTI from $[\mathbf{3}]^{2+}$ in hypoxia, highlights the strong potential of *trans* complexes for dual-targeting PACT.

4.4 Conclusion

In this study, the successful synthesis of three novel ruthenium-based PACT compounds was demonstrated based on the *trans*-$[Ru(MeL)(L')(L'')]^{2+}$ scaffold where the axial ligands L' and L'' were either identical or different protein inhibitors. Symmetric compounds $[\mathbf{1}]^{2+}$ and $[\mathbf{2}]^{2+}$ featured two equivalents of pyridine-based NAMPT inhibitor STF31 or two thioether-based tubulin polymerization inhibitor MTI, respectively. The preparation of the dissymmetric compound $[\mathbf{3}]^{2+}$, with L' = STF31 and L'' = MTI, was achieved by a red light-induced

photosubstitution reaction starting from [**1**]$^{2+}$ in the presence of 3 eq. MTI. In all three cases, photosubstitution of the axial ligands was demonstrated with ^{1}H-NMR and UV-Vis spectroscopy, and the photosubstitution quantum yields upon blue, green or red light irradiation were determined. Distinct differences in photoreactivity between the compounds were observed, with [**2**]$^{2+}$ being the only compound not reactive upon red-light irradiation. Moreover, the characteristic reactivity of the axial ligands in [**3**]$^{2+}$ allowed for selective photosubstitution first of STF31 upon red light irradiation, followed by MTI upon blue light irradiation. Compound [**3**]$^{2+}$ is the first compound allowing for controlled release of two different inhibitors by varying the irradiation wavelength, highlighting the potential of such *trans* complexes for PACT.

While no significant photoindexes were observed for the bis-MTI compound [**2**]$^{2+}$, the bis-(STF31) analogue [**1**]$^{2+}$ and the dissymmetric analogue bearing 1 eq. of each inhibitor, [**3**]$^{2+}$, became significantly more cytotoxic after green or red light activation in skin melanoma (A375) and lung cancer (A549) cells, both under normoxia and hypoxia. Independent on oxygen concentration, [**3**]$^{2+}$ showed no toxicity in the dark in U87MG glioblastoma cells (EC_{50} > 75 µM), while green or red light activation increased its toxicity significantly. Strikingly, [**3**]$^{2+}$ appeared to be more potent in hypoxic conditions than in normoxic conditions, with photoindexes increasing up to 3–fold. These exceptional results also indicate an oxygen-independent synergistic effect on cell viability upon photorelease of STF31 and MTI from [**3**]$^{2+}$. Though *in vivo* validation and further mechanistic investigation will be needed to assess NAMPT and microtubule inhibition, the exceptional *in vitro* properties of [**3**]$^{2+}$ under hypoxia underlines the high potential of such dual-targeting, *trans* PACT compounds for the treatment of hypoxic tumors.

4.5 Experimental

4.5.1 General information

Unless otherwise noted, all reagents and solvents were purchased from commercial suppliers (Fluorochem, Sigma-Aldrich, BLDPharm, VWR, TCI) and used without further purification. Compounds MeL and [**4**]$(PF_6)_2$ were synthesized according to the procedure reported in Chapter 3. STF-31 was prepared by Yurii Husiev as previously reported.[19] MTI was provided by Alexander Kornienko and prepared as previously reported.[16] Anhydrous and oxygen-free solvents were obtained using common drying (activated 4 Å molecular sieves) and degassing (freeze-pump-thaw method) procedures. The reactions were carried under air unless stated otherwise. Standard Schlenk techniques were used for the reactions that were carried out under an inert atmosphere. Filters used were Whatman® regenerated cellulose membrane filters, RC60 Membrane circles, diam. 47 mm, pore size 1 µm. TLCs were performed using either Supelco analytical silica gel on aluminium foils with fluorescence indicator 254 nm or Supelco analytical aluminum oxide 60 with fluorescence

indicator 254 nm. Column chromatography was carried on silica gel (40-63 µm) or on activated neutral aluminum oxide (Brockmann Grade I) from VWR Chemicals. The microwave tubes (product number: 351521) were purchased from Biotage (Uppsala, Sweden) and heated using Thermo Scientific™ Reacti-block™ T-1 (9 holes; dimensions: 17mm diameter × 45 mm deep). Size exclusion chromatography was performed using Cytiva Sephadex LH-20 (3 × 60 cm) as stationary phase. Anion exchange from hexafluorophosphate (PF_6) salts to the corresponding chloride salts was performed using DOWEX® 22 resin (3 × 11 cm) in methanol. Prior to the initial use, the resin was allowed to swell overnight in methanol. Additionally, the column was flushed with one column volume of 1 M HCl in methanol and washed with methanol until neutral pH. A 1 M HCl in methanol flush and methanol wash until neutral pH was done before every use to regenerate the resin. All synthesized ruthenium complexes were stored at room temperature and protected from light. NMR spectra were recorded on Bruker Avance 400 or 500 MHz and the FIDs were treated with MestReNova software. The chemical shifts are given relative to the residual signal of the solvent (Acetone-d6: δ (^{1}H) = 2.05 ppm, δ (^{13}C) = 29.84 ppm; $CDCl_3$: δ (^{1}H) = 7.26 ppm, δ (^{13}C) = 77.16 ppm; DMSO-d6: δ (^{1}H) = 2.50 ppm, δ (^{13}C) = 39.52 ppm), or relative to an external standard (TMS: δ (^{1}H) = 0 ppm, δ (^{13}C) = 0 ppm). The mass spectra (ESI-MS) were recorded in methanol (UPLC grade) with 1% (v/v) of formic acid on a Shimadzu LCMS-2020 (ESI-Q). High-resolution mass spectra (HRMS) were recorded on Thermo Finnigan LTQ Orbitrap.

4.5.2 Synthesis

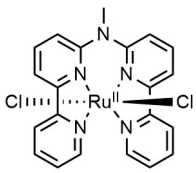

[Ru(**MeL**)Cl_2], **5**: A microwave tube was charged with N-([2,2'-bipyridin]-6-yl)-N-methyl-[2,2'-bipyridin]-6-amine **MeL** (400 mg, 1.18 mmol, 1.0 eq), dichloro(1,5-cyclooctadiene)ruthenium(II) (335 mg, 1.19 mmol, 1.01 eq), *o*-dichlorobenzene (4.7 mL) and a stirring bar. The tube was sealed with a septum containing crimp cap and the vessel was purged with N_2 for 15 min. Once purged, the mixture was stirred at 180 °C. After 48 h, the reaction mixture was allowed to cool to RT and the product precipitated upon addition of diethyl ether (100 mL). The precipitate was filtered over a membrane filter and washed with diethyl ether, toluene and pentane. Drying under high vacuum yielded the product as dark green powder (519 mg, 1.01 mmol, 86%). ^{1}H-NMR (400 MHz, DMSO-d_6) δ 9.64 (dd, *J* = 5.8, 1.5 Hz, 2H), 8.67 (dd, *J* = 8.2, 1.4 Hz, 2H), 8.38 (dd, *J* = 7.9, 0.9 Hz, 2H), 8.06 (td, *J* = 7.8, 1.4 Hz, 2H), 7.96 (t, *J* = 8.1 Hz, 2H), 7.73 (ddd, *J* = 7.2, 5.6, 1.3 Hz, 2H), 7.56 (dd, *J* = 8.5, 0.9 Hz, 2H), 3.96 (s, 3H). ^{13}C{H} NMR (101 MHz, DMSO-d_6) δ 159.05, 158.33, 154.64, 153.54, 135.61, 133.21, 124.71, 122.11, 116.33, 114.25, 43.83. ESI-MS: exact m/z calculated for $[C_{21}H_{17}N_5RuCl + CH_3OH]^{2+}$: 508.1 m/z, found: 507.1 m/z.

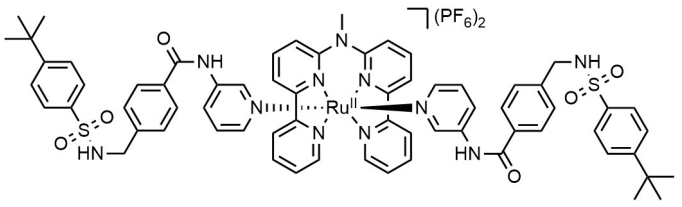

[Ru(**MeL**)(STF31)$_2$](PF$_6$)$_2$, [**1**](PF$_6$)$_2$: In a microwave tube **5** (101 mg, 0.20 mmol, 1.0 eq) was dissolved in water (0.5 mL), and purged with N_2 for 15 min. After stirring at 80 °C for 1 h, the solution was cooled to RT and STF31 (252 mg, 0.59 mmol, 3.0 eq) in methanol (4.5 mL) was added. The resulting mixture was stirred 80 °C and the solution changed color from black to dark red. The conversion was monitored with TLC (SiO_2, 10% methanol half-saturated with KPF_6 in DCM). After 48 h, the reaction was completed and the reaction mixture was allowed to cool to RT. The product was precipitated by addition of half-saturated aqueous KPF_6 solution, the suspension was filtered over a membrane filter and washed with minimal amount of water (5 mL) followed by diethyl ether (100 mL). The crude product was purified by size exclusion chromatography (LH-20 in acetone). The product-containing fractions were combined and concentrated *in vacuo*. After precipitation in diethyl ether and filtration over a membrane filter, drying under high vacuum yielded the product as red powder (188 mg, 0.12 mmol, 61%). ^{1}H-NMR (400 MHz, Acetone-*d*$_6$) δ 10.15 – 10.11 (m, 2H), 9.51 (s, 2H), 8.78 – 8.71 (m, 4H), 8.48 (dd, *J* = 7.9, 0.9 Hz, 2H), 8.36 – 8.29 (m, 4H), 8.16 (dd, *J* = 8.7, 0.9 Hz, 2H), 8.10 (ddd, *J* = 7.4, 5.7, 1.3 Hz, 2H), 7.78 – 7.70 (m, 12H), 7.62 – 7.57 (m, 4H), 7.42 (d, *J* = 8.3 Hz, 4H), 7.09 – 7.01 (m, 4H), 4.35 (s, 3H), 4.19 (d, *J* = 6.5 Hz, 4H), 1.33 (s, 18H). ^{13}C{H} NMR (101 MHz, Acetone-*d*$_6$) δ 206.18, 166.38, 158.74, 157.27, 156.62, 156.20, 154.08, 147.94, 144.73, 143.66, 139.60, 138.42, 138.20, 133.54, 128.76, 128.63, 128.56, 128.43, 127.61, 126.88, 126.23, 124.98, 119.29, 118.95, 47.10, 44.92, 31.32. ESI-MS: exact m/z calculated for $[C_{67}H_{67}N_{11}O_6S_2Ru]^{2+}$: 643.7 m/z, found: 643.9 m/z. Elemental analysis (%) for compound [**1**](PF$_6$)$_2$ ($C_{67}H_{67}F_{12}N_{11}O_6P_2RuS_2$), calculated C, 51.01; H, 4.28; N, 9.77; found C, 50.91; H, 4.17; N, 9.66. UV-Vis (1/1 acetone/H_2O): λ_{max} (ε) = 484 nm (8.3×10^3 $M^{-1}cm^{-1}$).

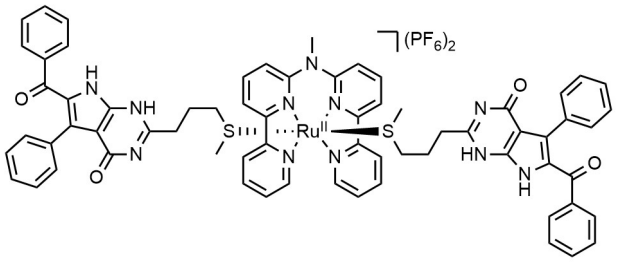

[Ru(**MeL**)(MTI)$_2$](PF$_6$)$_2$, [**2**](PF$_6$)$_2$: In a microwave tube **5** (75 mg, 0.15 mmol, 1.0 eq) was dissolved in water (1.0 mL), and purged with N_2 for 15 min. After stirring at 80 °C for 30 min, the solution was cooled to RT and MTI (125 mg, 0.31 mmol, 2.1 eq) in ethylene glycol (3.9 mL) was added. The resulting mixture was stirred at 120 °C and changed color from black to dark red. The conversion was monitored with TLC (SiO_2, 15% methanol half-saturated with KPF_6 in DCM). After 18 h, the reaction was completed and the mixture was allowed to cool to RT. The mixture was precipitated in half-saturated aqueous

KPF_6 solution, filtered over a membrane filter and washed with minimal amount of water (1 mL) followed by diethyl ether (50 mL). The crude product was purified by size-exclusion chromatography (LH-20 in acetone). The product-containing fractions were combined and concentrated *in vacuo*. After precipitation in diethyl ether and filtration over a membrane filter, drying under high vacuum yielded the product as pale brown powder (57 mg, 0.037 mmol, 24%). ^{1}H-NMR (500 MHz, Acetone-d_6) δ 11.33 (s, 2H), 10.45 (s, 2H), 9.79 (dd, *J* = 5.5, 1.3 Hz, 2H), 8.80 – 8.76 (m, 2H), 8.52 (dd, *J* = 8.0, 0.9 Hz, 2H), 8.31 (td, *J* = 7.8, 1.4 Hz, 2H), 8.26 (dd, *J* = 8.6, 7.7 Hz, 2H), 7.94 (ddd, *J* = 7.3, 5.6, 1.4 Hz, 2H), 7.85 (dd, *J* = 8.6, 0.9 Hz, 2H), 7.54 (dd, *J* = 8.3, 1.3 Hz, 4H), 7.36 – 7.31 (m, 7H), 7.17 – 7.12 (m, 5H), 7.11 – 7.05 (m, 7H), 4.12 (s, 3H), 2.47 (t, *J* = 6.5 Hz, 4H), 1.79 (t, *J* = 7.1 Hz, 4H), 1.70 (q, *J* = 6.9 Hz, 4H), 1.36 (s, 6H). ^{13}C{H} NMR (126 MHz, Acetone-d_6) δ 158.60, 158.33, 156.69, 155.99, 154.50, 140.11, 139.26, 138.48, 133.49, 132.76, 132.41, 130.25, 128.58, 128.46, 127.92, 125.62, 119.52, 118.86, 44.83, 34.20, 32.59, 23.54, 15.40. ESI-MS: exact m/z calculated for $[C_{67}H_{59}N_{11}O_4S_2Ru]^{2+}$: 623.7 m/z, found: 623.8 m/z. Elemental analysis (%) for compound [**2**]$(PF_6)_2$ ($C_{67}H_{59}F_{12}N_{11}O_4P_2RuS_2$), calculated C, 52.34; H, 3.87; N, 10.02; found C, 51.82; H, 4.04; N, 9.89. UV-Vis (1/1 acetone/H_2O): λ_{max} (ε) = 449 nm (6.5×10^3 $M^{-1}cm^{-1}$).

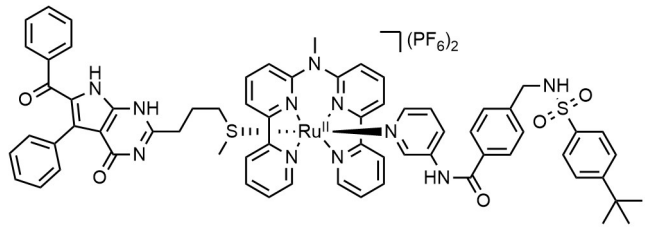

[Ru(**MeL**)(STF31)(MTI)]$(PF_6)_2$, [**3**]$(PF_6)_2$: [**1**]$(PF_6)_2$ (101 mg, 0.06 mmol, 1 eq) in acetone (50 mL) and MTI (78.4 mg, 0.19 mmol, 3 eq) in tetrahydrofuran (25 mL) were added under nitrogen to a 140 mL double-walled photoreactor with water cooling (see Figure I.1 and Appendix I for details). Acetone was added to a total volume of 125 mL and the reaction mixture was irradiated with a 650 nm LED lamp at RT while monitoring the reaction progress with TLC (SiO_2, 10% methanol half saturated with KPF_6 in DCM). After 1.5 h, the mixture was concentrated *in vacuo* and the product precipitated upon addition of diethyl ether. The precipitate was filtered over a membrane filter and washed with diethyl ether (50 mL). The crude product was purified by column chromatography (SiO_2, 10% methanol half saturated with KPF_6 in DCM). The product-containing fractions were combined and concentrated, followed by precipitation in half-saturated aqueous KPF_6 (100 mL). After filtration over a membrane filter, the product was washed with a minimal amount of water (1 mL) followed by diethyl ether (50 mL). Drying under high vacuum yielded the product as a brown/red powder (28 mg, 0.018 mmol, 28%). ^{1}H-NMR (500 MHz, Acetone-d_6) δ 11.35 (s, 1H), 10.53 (s, 1H), 10.01 (d, *J* = 5.6 Hz, 2H), 9.47 (s, 1H), 8.71 – 8.62 (m, 3H), 8.41 (d, *J* = 7.8 Hz, 2H), 8.28 (td, *J* = 7.8, 2.7 Hz, 4H), 8.07 (d, *J* = 8.5 Hz, 2H), 8.05 – 8.01 (m, 2H), 7.80 – 7.73 (m, 2H), 7.69 (d, *J* = 8.1 Hz, 2H), 7.63 – 7.56 (m, 3H), 7.56 – 7.50 (m, 2H), 7.45 (d, *J* = 5.6 Hz, 1H), 7.41 (d, *J* = 8.3 Hz, 2H), 7.32 (dq, *J* = 5.9, 3.9, 2.9 Hz, 3H), 7.14 (t, *J* = 7.6 Hz, 2H), 7.10 – 7.01 (m,

4H), 6.96 (dd, *J* = 8.4, 5.7 Hz, 1H), 4.28 (s, 3H), 4.19 (d, *J* = 6.6 Hz, 2H), 2.58 (t, *J* = 6.7 Hz, 2H), 1.84 – 1.75 (m, 2H), 1.58 (s, 3H), 1.33 (s, 9H). ^{13}C-NMR (126 MHz, Acetone-*d*$_6$) δ 166.35, 159.59, 158.77, 158.42, 156.89, 156.16, 154.24, 150.42, 146.52, 143.78, 143.08, 139.86, 138.98, 138.54, 133.51, 133.46, 132.68, 132.41, 130.19, 129.01, 128.67, 128.63, 128.54, 128.42, 127.86, 127.62, 126.89, 126.56, 125.12, 119.24, 119.13, 47.09, 44.63, 35.71, 32.85, 31.33, 23.94, 16.87. ESI-HRMS: exact m/z calculated for $[C_{67}H_{63}N_{11}O_5S_2Ru]^{2+}$: 633.6752 m/z, found: 633.6750 m/z. Elemental analysis (%) for compound [**3**]$(PF_6)_2$ ($C_{67}H_{63}F_{12}N_{11}O_5P_2RuS_2$), calculated C, 51.67; H, 4.28; N, 9.89; found C, 50.64; H, 4.50; N, 8.95. UV-Vis (1/1 acetone/H_2O): λ_{max} (ε) = 459 nm (6.5×10^3 $M^{-1}cm^{-1}$).

Anion exchange: The ruthenium complex of interest as hexafluorophosphate salt was dissolved in a minimum amount of acetone, and diluted with an equal amount of methanol. The solution was brought onto an anion exchange column and eluted with methanol. After collection of the colored fractions and concentration *in vacuo*, the product was precipitated in diethyl ether. Filtration over a membrane filter and drying under high vacuum provided the chloride salt of the product as a red powder. Anion exchange typically proceeded with a yield of around 95%.

[Ru(**MeL**)(STF31)$_2$]Cl_2, [**1**]Cl_2

^{1}H-NMR (400 MHz, MeOD) δ 9.90 (d, *J* = 5.6 Hz, 2H), 8.64 (d, *J* = 8.1 Hz, 2H), 8.50 (d, *J* = 2.3 Hz, 2H), 8.38 (d, *J* = 7.8 Hz, 2H), 8.24 (dt, *J* = 11.2, 7.6 Hz, 4H), 8.06 – 7.98 (m, 4H), 7.76 – 7.70 (m, 4H), 7.69 – 7.64 (m, 4H), 7.61 (ddd, *J* = 8.5, 2.3, 1.2 Hz, 2H), 7.57 – 7.53 (m, 4H), 7.40 (d, *J* = 5.5 Hz, 2H), 7.35 (d, *J* = 8.1 Hz, 4H), 6.95 (dd, *J* = 8.4, 5.6 Hz, 2H), 4.15 (s, 3H), 4.11 (s, 4H), 1.32 (s, 18H). ^{13}C{H} NMR (101 MHz, MeOD) δ 168.01, 159.17, 157.68, 157.47, 156.52, 154.23, 148.05, 144.83, 143.90, 139.87, 139.06, 138.80, 138.62, 133.90, 128.92, 128.76, 127.87, 127.16, 126.35, 125.37, 119.36, 119.27, 47.27, 44.49, 31.46. ESI-MS: exact m/z calculated for $[C_{67}H_{67}N_{11}O_6S_2Ru]^{2+}$: 643.7 m/z, found: 643.8 m/z. Elemental analysis (%) for compound [**1**]Cl_2 ($C_{67}H_{67}Cl_2N_{11}O_6RuS_2$), calculated C, 59.24; H, 4.97; N, 11.34; found C, 59.31; H, 4.92; N, 11.24.

[Ru(**MeL**)(MTI)$_2$]Cl_2, [**2**]Cl_2:

^{1}H NMR (600 MHz, MeOD) δ 9.54 (dt, *J* = 5.7, 1.1 Hz, 2H), 8.57 (dd, *J* = 8.1, 1.3 Hz, 2H), 8.32 – 8.28 (m, 2H), 8.17 (td, *J* = 7.8, 1.3 Hz, 2H), 8.12 – 8.08 (m, 2H), 7.84 (ddd, *J* = 7.2, 5.5, 1.3 Hz, 2H), 7.59 (d, *J* = 8.5 Hz, 2H), 7.57 – 7.55 (m, 4H), 7.36 – 7.31 (m, 6H), 7.16 – 7.10 (m, 10H), 3.90 (s, 3H), 2.44 – 2.37 (m, 4H), 1.69 – 1.61 (m, 4H), 1.54 (t, *J* = 7.0 Hz, 4H), 1.20 (s, 6H). ^{13}C{H} NMR (151 MHz, MeOD) δ 190.39, 161.54, 158.58, 158.53, 156.97, 156.08, 154.59, 151.01, 140.36, 139.66, 138.59, 133.72, 133.35, 132.63, 130.74, 129.42, 129.03, 128.93, 128.65, 128.53, 128.46, 125.80, 119.70, 118.71, 106.04, 44.67, 34.33, 32.06, 23.08, 15.37. ESI-MS: exact m/z calculated for $[C_{67}H_{59}N_{11}O_4S_2Ru]^{2+}$: 623.7 m/z, found: 623.8 m/z.

[Ru(**MeL**)(STF31)(MTI)]Cl_2, [**3**]Cl_2:

^{1}H-NMR (500 MHz, MeOD) δ 9.78 (d, *J* = 5.7 Hz, 2H), 8.47 (d, *J* = 8.1 Hz, 2H), 8.42 (d, *J* = 2.4 Hz, 1H), 8.22 (d, *J* = 7.8 Hz, 2H), 8.16 (q, *J* = 8.2 Hz, 4H), 7.95 (t, *J* = 6.7 Hz, 2H), 7.89 (d, *J* = 8.5 Hz, 2H), 7.73 (d, *J* = 8.3 Hz, 2H), 7.64 (d, *J* = 8.1 Hz, 2H), 7.55 (dd, *J* = 7.8, 4.4 Hz, 5H), 7.49 (d, *J* = 8.3 Hz, 1H), 7.33 (dt, *J* = 11.5, 7.8 Hz, 5H), 7.22 (d, *J* = 5.6 Hz, 1H), 7.16 – 7.07 (m, 6H), 6.86 (dd, *J* = 8.4, 5.6 Hz, 1H), 4.11 (d, *J* = 3.4 Hz, 5H), 2.52 (t, *J* = 6.2 Hz, 2H), 1.84 (s, 2H), 1.75 (s, 2H), 1.45 (s, 3H), 1.32 (s, 10H). ^{13}C{H} NMR (126 MHz, MeOD) δ 168.06, 161.56, 158.76, 157.26, 156.47, 154.37, 146.72, 144.10, 143.22, 140.17, 139.40, 138.98, 138.68, 133.81, 133.75, 133.68, 133.31, 132.61, 130.63, 129.36, 128.93, 128.73, 128.50, 127.88, 127.17, 126.67, 125.33, 119.38, 119.21, 47.26, 44.39, 36.12, 32.47, 31.47, 17.03. ESI-MS: exact m/z calculated for $[C_{67}H_{63}N_{11}O_5S_2Ru]^{2+}$: 633.7 m/z, found: 633.8 m/z. Elemental analysis (%) for compound [**3**]Cl_2 ($C_{67}H_{63}Cl_2N_{11}O_5RuS_2$), calculated C, 59.24; H, 4.97; N, 11.34; found C, 59.94; H, 4.66; N, 11.32.

[Ru(**MeL**)(Py)(MTE)]Cl_2, [**4**]Cl_2:

^{1}H-NMR (400 MHz, MeOD) δ 9.85 (dd, *J* = 6.1, 1.2 Hz, 2H), 8.58 (d, *J* = 7.8 Hz, 2H), 8.34 (dd, *J* = 7.9, 1.0 Hz, 2H), 8.31 – 8.21 (m, 4H), 8.02 (ddd, *J* = 7.3, 5.6, 1.4 Hz, 2H), 7.97 (dd, *J* = 8.5, 1.0 Hz, 2H), 7.53 (tt, *J* = 7.7, 1.5 Hz, 1H), 7.48 (dt, *J* = 5.1, 1.5 Hz, 2H), 6.95 – 6.87 (m, 2H), 4.14 (s, 3H), 1.90 (t, *J* = 5.7 Hz, 2H), 1.46 (s, 3H).^{13}C{H} NMR (101 MHz, MeOD) δ 158.91, 157.40, 156.56, 154.54, 151.90, 140.19, 139.36, 128.91, 127.07, 125.36, 119.44, 119.29, 58.98, 44.23, 40.29, 17.71. ESI-HRMS: exact m/z calculated for $[C_{29}H_{30}N_6O_1S_1Ru]^{2+}$: 306.0617 m/z, found: 306.0619 m/z. Elemental analysis (%) for compound [**4**]Cl_2 ($C_{29}H_{30}Cl_2N_6ORuS$), calculated C, 51.03; H, 4.43; N, 12.31; found C, 49.99; H, 4.70; N, 11.94.

4.5.3 Photochemistry

Photosubstitution followed by ^{1}H-NMR

The ^{1}H-NMR photosubstitution experiments were performed as described in appendix I.2.5. Results for the compounds reported in this chapter are provided in appendix IV.2.3.

Molar absorption coefficient determination

Molar absorption coefficients were determined as described in appendix I.2.1. Results for the compounds reported in this chapter are provided in appendix IV.1.1.

Photosubstitution quantum yield measurements

Photon fluxes of all LEDs were determined using ferrioxalate actinometry and is described in detail in appendix I. The photosubstitution quantum yields were determined as described in appendix I, and the results are reported in appendix IV.1.2.

Singlet oxygen generation quantum yield measurements

The emission spectra were recorded, and the corresponding singlet oxygen generation quantum yields determined as described in appendix I.2.4. The emission spectra and data are reported in appendix IV.1.3.

UV-Vis absorbance evolution in OptiMEM media ("mock irradiation")

To model what happens in cell culture conditions, compounds [**1**]Cl_2, [**2**]Cl_2 or [**3**]Cl_2 were dissolved in DMSO and further diluted with OptiMEM complete (OptiMEM supplemented with 2.5% v/v fetal calf serum, 0.1% v/v penicillin/streptomycin, and 1.0% v/v Glutamine-S) to a final concentration of 5.0×10^{-5} M with 0.14% DMSO. The compound solution were transferred to a 96-well plate (flat base; Sarstedt; v = 200 µL per well) and irradiated at different time intervals with green light (520 ± 35 nm; 17.1 mW/cm^2; t = 0, 2.5, 5, 7.5, 10, 12.5, 15, 20, 25 and 30 minutes) or red light (630 ± 24 nm; 31.3 mW/cm^2; t = 0, 5, 10, 15, 20, 25, 30, 40, 50 and 60 minutes). The absorbance between 300 and 800 nm was measured by a M1000 Tecan reader. Averaging the absorbance of a technical triplicate and baseline subtraction provided the resulting spectra reported in appendix IV.5.

4.5.4 Cell viability assay

Experimental details of cell culturing, cytotoxicity and cell irradiation are described in appendix I.3. The results are reported in detail in appendix IV.2.

4.5.5 Combination index calculations

The combination indexes were calculated based on the method by Chou and Talalay using the CompuSyn software (free download after registration; www.combosyn.com).[23] The method is based on the median-effect equation derived from the mass-action law principle, as shown equation 4.1:

$$\frac{f_a}{f_u} = \left(\frac{D}{D_m}\right)^m \tag{4.1}$$

where f_a is the affected fraction (metabolic activity inhibition compared to untreated wells), f_u is the unaffected fraction ($f_u = 1 - f_a$), D is the dose of the drug (in µM), D_m is the median-effect dose (in µM), and m is the slope of the dose-response curve. Because evaluated mixture of STF31:MTI was kept at a 1:1 ratio, the CI values can be calculated for each effect according equation 4.2:

$$CI = (D_{mix})_{f_a} \cdot \left(\frac{1}{(D_{STF31})_{f_a}} + \frac{1}{(D_{MTI})_{f_a}}\right) \tag{4.2}$$

where $(D_{mix})_{f_a}$ is the dose (in µM) of the mixture (STF-31:MTI, or of green light-activated [**3**]$^{2+}$) to achieve an effect f_a and $(D_x)_{f_a}$ is the dose (in µM) of a single drug x (STF-31 or MTI) to achieve the same effect f_a.

4.5.6 Cellular uptake

Materials and instrumentation

65% Nitric acid (Suprapur, Merck) was used in the sample digestion process, while diluted 1% nitric acid (v/v) was employed as a carrying solution throughout the ICP measurements. For preparation of calibration and internal standards National Institute of Standards and Technology (NIST)-traceable 1000 mg/L elemental standards were used (TraceCERT, Fluka). Approximately 18 MΩ cm^{-1} water (Milli-Q) was employed in all sample preparation and analysis steps. Calibration standards were prepared in a Secuflow fume hood (SCALA) to prevent contamination by atmospheric particulates. The standard samples and measurement samples were analyzed for trace elements using the NexION 2000 (PerkinElmer) ICP-MS instrument equipped with a concentric glass nebulizer and Peltier-cooled glass spray chamber. An SC2 DX autosampler (PerkinElmer) was connected to the ICP-MS for sample introduction. Syngistix software for ICP-MS (v.2.5, PerkinElmer) was used for all data recording and processing. Five trace elemental calibration standards for ICP-MS analysis were prepared using NIST-traceable 1000 mg/L Ru standards: 0, 1, 5, 20, and 100 µg/L. Samples were analyzed without dilution in the original delivery containers to minimize the possibility of contamination. Here, 10 µg/L Rh and In were used as internal standards. To check the calibration, samples were analyzed with a blank measurement and a repeat measurement of one of the calibration standards. For the calibration curve, the accepted correlation coefficient (Cor.Coeff) was to be found higher than 0.999.

Determination of cellular ruthenium content

Cellular ruthenium content in A375 (normoxic and hypoxic), U87MG (normoxic and hypoxic) and U251 (normoxic) cells was determined by ICP-MS. The cells were seeded (density = 175×10^3 cells/well for A375 and U251; 200×10^3 cells/well for U87MG) in OptiMEM complete media (1 mL) in 12-well transparent plates (Sarstedt, #83.3921.500) at t = 0 h and incubated at 37°C. After 24h, 1 mL of the compound solution was added (final concentrations: [**1**]Cl_2 = 2 µM; [**2**]Cl_2 = 0.5 µM; [**3**]Cl_2 = 1 µM for A375, 5 µM for U87MG NX, 10 µM for U87MG HX and U251). At t = 72 h, the medium was aspirated and the well washed with 1 mL PBS. After trypsinization of the cells (1 mL for 1 min), OptiMEM complete (900 µL) was added and the cell suspension was transferred to a 1.5 mL Eppendorf tube. Trypan blue (10 µL) and the cell suspension (10 µL) were mixed, and the cells were counted using a BioRad TC20™ automated cell counter. The cell suspension was centrifuged (5 min at 1×10^5 rpm), the supernatant removed, and the pellet was washed twice with PBS (2 × 1 mL). To digest the cells, the cell pellet was dissolved in 65% nitric acid (500 µL), transferred to glass test tube covered with a marble and incubated in an oven at 95 °C overnight. The resulting solution was transferred to a 15 mL corning tube (Sarstedt) and diluted with MilliQ water to a total volume of 10 mL (~3.2% HNO_3). The Ru content was analyzed by ICPMS. The amount of ruthenium taken up by cells was calculated and is reported in Table IV.3. The reported values are the mean with standard deviation of three individual experiments.

4.6 References

(1) Mokhtari, R. B.; Homayouni, T. S.; Baluch, N.; Morgatskaya, E.; Kumar, S.; Das, B.; Yeger, H. Oncotarget **2017**, *8*, 38022.

(2) Al-Lazikani, B.; Banerji, U.; Workman, P. Nat Biotechnol **2012**, *30*, 679.

(3) Nair, N. U.; Greninger, P.; Zhang, X.; Friedman, A. A.; Amzallag, A.; Cortez, E.; Sahu, A. D.; Lee, J. S.; Dastur, A.; Egan, R. K.; Murchie, E.; Ceribelli, M.; Crowther, G. S.; Beck, E.; McClanaghan, J.; Klump-Thomas, C.; Boisvert, J. L.; Damon, L. J.; Wilson, K. M.; Ho, J.; Tam, A.; McKnight, C.; Michael, S.; Itkin, Z.; Garnett, M. J.; Engelman, J. A.; Haber, D. A.; Thomas, C. J.; Ruppin, E.; Benes, C. H. Nat Commun **2023**, *14*, 3830.

(4) Jaaks, P.; Coker, E. A.; Vis, D. J.; Edwards, O.; Carpenter, E. F.; Leto, S. M.; Dwane, L.; Sassi, F.; Lightfoot, H.; Barthorpe, S.; Van Der Meer, D.; Yang, W.; Beck, A.; Mironenko, T.; Hall, C.; Hall, J.; Mali, I.; Richardson, L.; Tolley, C.; Morris, J.; Thomas, F.; Lleshi, E.; Aben, N.; Benes, C. H.; Bertotti, A.; Trusolino, L.; Wessels, L.; Garnett, M. J. Nature **2022**, *603*, 166.

(5) Fan, K.; Cheng, L.; Li, L. Briefings in Bioinformatics **2021**, *22*, bbab271.

(6) Qu, C.-P.; Sun, G.-X.; Yang, S.-Q.; Tian, J.; Si, J.-G.; Wang, Y.-F. Medicine **2017**, *96*, e5797.

(7) Wu, D.; Pusuluri, A.; Vogus, D.; Krishnan, V.; Shields, C. W.; Kim, J.; Razmi, A.; Mitragotri, S. Journal of Controlled Release **2020**, *323*, 36.

(8) Jangili, P.; Won, M.; Kim, S. J.; Chun, J.; Shim, I.; Kang, C.; Ren, W. X.; Kim, J. S. ACS Appl. Bio Mater. **2019**, *2*, 3532.

(9) Sharma, A.; Chun, J.; Ji, M. S.; Lee, S.; Kang, C.; Kim, J. S. ACS Appl. Bio Mater. **2021**, *4*, 2026.

(10) Bonnet, S. J. Am. Chem. Soc. **2023**, *145*, 23397.

(11) Havrylyuk, D.; Hachey, A. C.; Fenton, A.; Heidary, D. K.; Glazer, E. C. Nat. Commun. **2022**, *13*, 3636.

(12) Respondek, T.; Garner, R. N.; Herroon, M. K.; Podgorski, I.; Turro, C.; Kodanko, J. J. J. Am. Chem. Soc. **2011**, *133*, 17164.

(13) Filevich, O.; Etchenique, R. Photochem Photobiol Sci **2013**, *12*, 1565.

(14) He, G.; He, M.; Wang, R.; Li, X.; Hu, H.; Wang, D.; Wang, Z.; Lu, Y.; Xu, N.; Du, J.; Fan, J.; Peng, X.; Sun, W. Angew Chem Int Ed **2023**, *62*, e202218768.

(15) Bretin, L.; Husiev, Y.; Ramu, V.; Zhang, L.; Hakkennes, M.; Abyar, S.; Johns, A. C.; Le Dévédec, S. E.; Betancourt, T.; Kornienko, A.; Bonnet, S. Angew Chem Int Ed **2024**, *63*, e202316425.

(16) Medellin, D. C.; Zhou, Q.; Scott, R.; Hill, R. M.; Frail, S. K.; Dasari, R.; Ontiveros, S. J.; Pelly, S. C.; Van Otterlo, W. A. L.; Betancourt, T.; Shuster, C. B.; Hamel, E.; Bai, R.; LaBarbera, D. V.; Rogelj, S.; Frolova, L. V.; Kornienko, A. J. Med. Chem. **2016**, *59*, 480.

(17) Kraus, D.; Reckenbeil, J.; Veit, N.; Kuerpig, S.; Meisenheimer, M.; Beier, I.; Stark, H.; Winter, J.; Probstmeier, R. Cell Oncol. **2018**, *41*, 485.

(18) Van Rixel, V. H. S.; Ramu, V.; Auyeung, A. B.; Beztsinna, N.; Leger, D. Y.; Lameijer, L. N.; Hilt, S. T.; Le Dévédec, S. E.; Yildiz, T.; Betancourt, T.; Gildner, M. B.; Hudnall, T. W.; Sol, V.; Liagre, B.; Kornienko, A.; Bonnet, S. J. Am. Chem. Soc. **2019**, *141*, 18444.

(19) Lameijer, L. N.; Ernst, D.; Hopkins, S. L.; Meijer, M. S.; Askes, S. H. C.; Le Dévédec, S. E.; Bonnet, S. Angew. Chem. Int. Ed. **2017**, *56*, 11549.

(20) Snellenburg, J. J.; Laptenok, S. P.; Seger, R.; Mullen, K. M.; Stokkum, I. H. M. V. J. Stat. Soft. **2012**, *49*.

(21) *The IUPAC Compendium of Chemical Terminology: The Gold Book*; Gold, V., Ed.; 4th ed.; International Union of Pure and Applied Chemistry (IUPAC): Research Triangle Park, NC, **2019**.

(22) Bae, S.-K.; Kim, S.-R.; Kim, J. G.; Kim, J. Y.; Koo, T. H.; Jang, H.-O.; Yun, I.; Yoo, M.-A.; Bae, M.-K. FEBS Letters **2006**, *580*, 4105.

(23) Chou, T.-C.; Talalay, P. Advances in Enzyme Regulation **1984**, *22*, 27.

(24) Garner, R. N.; Gallucci, J. C.; Dunbar, K. R.; Turro, C. Inorg. Chem. **2011**, *50*, 9213.

(25) Sgambellone, M. A.; David, A.; Garner, R. N.; Dunbar, K. R.; Turro, C. J. Am. Chem. Soc. **2013**, *135*, 11274.

(26) Doroshow, J. H.; Simon, R. M. Cell **2017**, *171*, 1476.
(27) Harkcom, W. T.; Ghosh, A. K.; Sung, M. S.; Matov, A.; Brown, K. D.; Giannakakou, P.; Jaffrey, S. R. Proc. Natl. Acad. Sci. U.S.A. **2014**, *111*.
(28) Jing, X.; Yang, F.; Shao, C.; Wei, K.; Xie, M.; Shen, H.; Shu, Y. Mol Cancer **2019**, *18*, 157.
(29) Al-Mehdi, A.-B.; Pastukh, V. M.; Swiger, B. M.; Reed, D. J.; Patel, M. R.; Bardwell, G. C.; Pastukh, V. V.; Alexeyev, M. F.; Gillespie, M. N. Sci. Signal. **2012**, *5*.
(30) Sharma, P.; Xu, J.; Williams, K.; Easley, M.; Elder, J. B.; Lonser, R.; Lang, F. F.; Lapalombella, R.; Sampath, D.; Puduvalli, V. K. Neuro-Oncology **2022**, *24*, 229.